CALCULATION OF BULK MATERIAL ELECTRONIC BAND STRUCTURE USING MATRIX MECHANICS: A PEDAGOGICAL APPROACH

by

Robert Lee Pavelich

A thesis submitted in partial fulfillment of the requirements for the degree of

Master of Science

Department of Physics

University of Alberta

Abstract

We present a method, intended primarily for pedagogical purposes, to extend the one-dimensional Kronig-Penney model (the standard starting point for solid-state physics) to the case of arbitrary potential shapes and to higher dimensions using matrix mechanics. We generate, either analytically or numerically, the matrix elements for a unit cell of some potential which can then be diagonalized to give the energies and eigenstates. Bloch's theorem can be introduced as purely additive non-potential-dependent terms on the main diagonal which allows us to "sweep out" the band structure at virtually no additional cost. In one-dimension our results correspond exactly with the known analytical solutions to the Kronig-Penney model, and in higher dimensions our results match the usual shallow and deep well limits, namely the nearly free electron model and the tight binding model respectively. Our method has the advantage of using only concepts familiar to a senior quantum mechanics student, lending it conceptual simplicity and clarity. This provides a tool for senior undergraduates and beginning graduate students to generate their own band structures, allowing for a tight coupling between computational exploration and intuition formation.

Preface
(Mandatory due to collaborative work)

Significant portions of Chapters 2 and 3 of this monograph have been published as R. L. Pavelich and F. Marsiglio, "The Kronig-Penney model extended to arbitrary potentials via numerical matrix mechanics," *American Journal of Physics*, vol. 83, issue 9, 773–781. Also, significant portions of Chapter 4 are from the working paper R. L. Pavelich and F. Marsiglio, "Calculation of 2D electronic band structure using matrix mechanics," which is undergoing peer review at the time of this writing. For both papers, I was responsible for the research, computations, and manuscript composition. F. Marsiglio was the supervisory author and was involved in both the research and manuscript composition.

To all my teachers, past and present
look ye on what you have wrought, and despair

Acknowledgments

No work of sufficient magnitude is entirely the product of one mind, and this monograph is no exception. First and foremost I would like to extend many thanks to my adviser Frank Marsiglio who has guided me in every step of this research. He has unfailingly made himself available to give advice, suggestions, and direction for which I am very grateful. I would also like to thank the committee members overseeing this research, namely Lyndsay LeBlanc and Richard Sydora, without whom this would just be a weird hobby.

I would also like to thank Tyler Dauphinee, who has been a consistent sounding board for ideas, particular for Section 3.6; Jayson Vavrek, who assisted me in some early Mathematica calculations; and Jeremy Burns, who helped me prepare some of the figures.

Reed Davis and Chris Marsh read drafts of this monograph. Their suggestion to make the writing style less readable and more obnoxious was ignored. Kevin Breton pointed out some typesetting errors, thus finally returning the favour.

Part of this monograph has already been published as a paper in the *American Journal of Physics*. I'd like to thank both the editor, David Schroeder, and the anonymous referees for their comments, criticisms, and suggestions.

On the suggestion of John Hopfield, Sanjoy Mahajan wrote his PhD dissertation in the form of a textbook [22]. That idea has always stuck in my head, and its influence can likely be felt throughout this monograph.

Contents

List of Tables

List of Figures

Chapter 1

Introduction

In this chapter we show where this monograph fits into an existing research programme, the principal research questions and goals, and discuss the structure of the rest of the monograph.

1.1 Background

Typical Approach to Solid-State Physics

The Kronig-Penney model [1] is the paradigmatic system for the demonstration of energy bands, separated by gaps, in crystalline solids. Comprised of a periodic array of rectangular wells (or barriers depending on how you look at it), it is convenient insofar as solutions to Schrödinger's equation are only required for regions of constant potential. Furthermore, the Kronig-Penney model serves as an enlightening illustration of the application of Bloch's theorem [2], which can seem abstract in isolation. This model is solvable analytically. One particularly important limit of the model, the so-called Dirac comb, comes about when the barriers decrease in width but increase in height. Taken to the limit, these barriers become infinitely thin and infinitely high (i.e., a periodic series of δ-potentials).

That is usually about as far as it goes in a senior quantum mechanics textbook (see for example Griffiths (2005) [3] who solves the Dirac comb case). In senior solid-state physics textbooks or beginning graduate condensed-matter textbooks (some canonical examples are [4, 5] while [6] is an interesting case of focusing just on electronic band structure) the typical approach comes in three steps:

1. The empty lattice approximation: The crystalline solid has no perturbative effect on the dynamics of the electrons. The energy bands take on the purely

parabolic shape of the free electron.

2. The nearly free electron model: A weak, periodic perturbative potential is introduced which causes a lifting of degeneracies in the electron bands forming band gaps. This presentation is usually fairly qualitative, with calculations of specific quantities only performed for highly specific weak potentials at points of high symmetry in reciprocal lattice space.

3. The tight binding model: Attention is then usually shifted to the opposite extreme, where electrons are tightly bound to the lattice atoms, with only a small overlap in the wavefunctions between neighboring atoms. These overlaps are used to calculate the so-called "hopping integrals" t and represents a probability amplitude for an electron to tunnel into the neighbouring well ($t \to 0$ corresponds to the case where the electron stays on the target atom forever and the bands are perfectly flat). Tight binding models can include just nearest-neighbor effects, next-nearest neighbor effects, and so on.

So what if, anything, is wrong with this standard treatment? One problem is that after taking such a course the student is still not equipped with the tools to calculate the electronic band structure for some arbitrary particular potential. Intermediate-strength potentials between the nearly free electron model and tight binding remain unexplored. The extent to which a potential with wells of some particular depth is adequately approximated by tight binding is also not addressed.

Tight binding can also appear suspicious and mysterious to the beginning student. For one, it involves expansions in hydrogenic orbitals (the "linear combination of atomic orbitals" or LCAO expansion). But this already begins to break down for the case of helium [12] (see the entry for Hutchison, Baker, and Marsiglio (2013) in the next subsection), so the student might reasonably wonder how it can be valid for, say, sodium. Furthermore, in standard treatments the hopping integral t isn't usually calculated directly, as the main focus is on deriving the functional form of the energy with respect to the reciprocal lattice vector K. This can make the whole presentation a bit bewildering.

After this, there's a large conceptual jump to numerical (black box) methods for realistic electronic band structure calculations. One popular program for these calculations is Wannier90 [37].

Matrix Mechanics Research Programme

In a 2009 paper "The harmonic oscillator in quantum mechanics: A third way" [8] Marsiglio presented a novel matrix mechanics method to solve one-dimensional potentials like the harmonic oscillator. While the matrix mechanics formulation of quantum mechanics dates back to 1925 (see [7] for an engaging history), the lack of computational speed for many decades limited the extent to which an individual student could investigate systems involving large matrices. Modern computers, though, have fast processors and large memories, and particularly when combined with sophisticated mathematics packages like Mathematica [30] and MATLAB [32], allow for individual students with relatively little prior programming experience to investigate more sophisticated quantum systems.

In collaboration with a number of students, Marsiglio has continued to extend this research programme of using matrix mechanics to explore problems in quantum mechanics understandable to undergraduate students. A number of published journal articles have been produced thus far:

- **2009** – "The harmonic oscillator in quantum mechanics: A third way," by Frank Marsiglio [8].
  The original paper of the research programme. Potentials of interest, like the harmonic oscillator or step function, are embedded in an infinite square well with a matrix mechanics expansion using the infinite square well basis states applied. For sufficiently centralized wavefunctions (low energy states) that don't "touch" the embedding walls of the infinite square well, this gives excellent agreement with analytical solutions.

- **2012** – "The double-well potential in quantum mechanics: a simple, numerically exact formulation," by Vedran Jelic and Frank Marsiglio [9].
  Extending the method of the first paper, this paper looks at double wells of various shapes. Excellent agreement was found with the WKB approximation.

- **2012** – "Why is the ground-state electron configuration for lithium $1s^2 2s$?" by W Stacey and Frank Marsiglio. [10]
  The ground state of the three-electron lithium atom is the $1s^2 2s$ state, not the $1s^2 2p$ state as one would naively expect. The traditional argument for why this is (given in textbooks such as Ref. [3]) is due to electron screening by the $1s$ electrons. In this paper, Stacey and Marsiglio use matrix mechanics with the radial equation to show that this traditional argument is flawed.

- **2013** – "Solving for three-dimensional central potentials using numerical matrix methods," by Bernadine Jugdutt and Frank Marsiglio [11].
  While the previous papers examined potentials in one-dimension, this one extended the method to three-dimensional systems like the Coulomb and Yukawa potentials. These can of course be rendered into a one-dimensional form of a radial equation with spherical harmonics reintroduced ex post.

- **2013** – "The spectral decomposition of the helium atom two-electron configuration in terms of hydrogenic orbitals," by Joel Hutchison, Marc Baker, and Frank Marsiglio [12].
  While the standard treatment has the elements of the periodic table represented in terms of hydrogenic orbitals (s, p, d, etc. orbitals), this paper showed that even for just helium a non-trivial contribution to the wavefunction comes from unbound continuum states.

- **2015** – "The importance of basis states: an example using the hydrogen basis," by Lindsey Forestell and Frank Marsiglio [13].
  Like the previous paper, in this paper it was shown that continuum states were required even for $Z > 1$ hydrogenic atoms.

- **2015** – "The Kronig-Penney model extended to arbitrary potentials via numerical matrix mechanics," by Robert Lee Pavelich and Frank Marsiglio [14].
  Matrix mechanics with periodic boundary conditions and Bloch's theorem applied to periodic potentials. This paper forms the basis for Chapters 2 and 3 of this monograph.

- **2015** – "Asymmetric wave functions from tiny perturbations," by Tyler Dauphinee and Frank Marsiglio [15].
  While the Jelic and Marsiglio (2012) paper dealt with symmetric double wells, in this paper tiny asymmetric perturbations were introduced. Remarkably, this caused the wavefunction to rapidly collapse nearly entirely into one or the other wells with extremely small perturbations.

- **2016?** – "Calculation of 2D electronic band structure using matrix mechanics," by Robert Lee Pavelich and Frank Marsiglio [16].
  This extends the Pavelich and Marsiglio (2015) paper to the case of two-dimensional periodic systems, and forms the basis of Chapter 4 of this monograph. Unpublished at the time of this writing.

- **2016?** – "Two and three particles interacting in a one-dimensional trap," by MengXing Na and Frank Marsiglio [17].
  In this paper, the matrix mechanics method was further extended to interacting particles in infinite square well and harmonic oscillator traps. Unpublished at the time of this writing.

This present work can therefore be understood as one part of a larger research programme aiming to significantly extend the toolkit of undergraduate and beginning graduate students in quantum mechanics. The particular emphasis of this monograph and the papers that serve as its foundation is solid-state systems.

1.2   Research Questions

The overriding questions shaping this research are as follows:

1. Can a matrix mechanics approach, hitherto confined to finite potentials, be extended to a periodic lattice (using Bloch's theorem) of arbitrary unit cell potentials?

2. If so, can such an approach be extended to higher dimensions?

3. Are there tangible advantages to using such an approach over orthodox methods (nearly free electron model and tight binding)?

Ultimately, we hope that we can construct a useful tool to deepen students' understanding of electronic band structure, as it has the author's. The efficacy won't ultimately be known until subsequent students try it for themselves.

1.3   Structure of This Monograph

In this introduction we have tried to show how this work fits into a wider research programme and why it would be a useful extension of the beginning solid-state physicist's toolkit. In Chapter 2 we will go over some mathematical preliminaries of the method, introducing the notation used throughout this monograph, and show the first step moving from one-dimensional potentials in an infinite square well as in the Marsiglio (2009) paper to periodic potentials. Further, we briefly review the Kronig-Penney model and Bloch's theorem so that this work is reasonably self-contained.

In Chapter 3 we then show how to introduce Bloch's theorem to the method conveniently, which then allows us to explore a variety of one-dimensional periodic

potentials. We begin comparisons of our numerical results to the canonical Kronig-Penney model before broadening our exploration to non-rectangular unit cell wells. In Chapters 4 and 5 we extend this to two-dimensional and three-dimensional systems respectively. Then in Chapter 6 we address remaining unsolved problems involving "zone unfolding" of band structures and the introduction of electric and magnetic fields.

Finally, we summarize what we have found with concluding remarks in Chapter 7, and suggest a possible curriculum outline to fit this work into quantum mechanics courses.

Chapter 2

Mathematical Preliminaries

In this chapter we go over the methodology behind our matrix mechanics approach. We lay out the methodology described in [8] for some potential embedded in an infinite square well and modify that to an embedding potential of periodic boundary conditions, and compare the two. We also review Bloch's theorem and the Kronig-Penney model briefly. If the reader is already well acquainted with matrix mechanics, a brief skim is still useful as we establish our notation.

2.1 Matrix Mechanics

Consider some potential of interest $V(x)$. The general procedure is to:

1. Embed $V(x)$ in some other simple potential $V_{\mathrm{emb}}(x)$ with known basis states.

2. Solve for the Hamiltonian matrix elements using the embedding potential basis states.

3. Truncate the infinite matrix to some manageable size that gives acceptable convergence.

4. Diagonalize the truncated matrix to produce the energies and eigenvalues.

The reader can see that this is an advantageous procedure pedagogically, as it only requires knowledge of linear algebra and integral calculus (plus access to a matrix diagonalization routine or the programming ability to craft one).

We begin by reviewing the first case explored in [8], which uses an infinite square well embedding potential (also referred to as open boundary conditions). Then we replace this embedding potential with periodic boundary conditions.

2.1.1 Infinite Square Well

We start with the infinite square well defined as

$$V_{\text{inf}}(x) = \begin{cases} 0 & 0 < x < a, \\ \infty & \text{otherwise,} \end{cases} \tag{2.1}$$

with a Hamiltonian given by

$$H_0 = -\frac{\hbar^2}{2m_0}\frac{\mathrm{d}^2}{\mathrm{d}x^2} + V_{\text{inf}}(x) \tag{2.2}$$

which has eigenstates

$$\psi_n(x) = \begin{cases} \sqrt{\frac{2}{a}}\sin\left(\frac{n\pi}{a}x\right) & 0 < x < a, \\ 0 & \text{otherwise,} \end{cases} \tag{2.3}$$

and eigenvalues

$$E_n^{(0)} = \frac{n^2\pi^2\hbar^2}{2m_0 a^2} \equiv n^2 E_1^{(0)}, \tag{2.4}$$

where a is the width of the well. Note that we have used notation from perturbation theory for $E_n^{(0)}$.

We now introduce our potential of interest $V(x)$ which is defined for $0 < x < a$ such that our full Hamiltonian is

$$H = H_0 + V(x) \tag{2.5}$$

where H_0 is from Eq. (2.2).Schrödinger's equation in ket notation is given as

$$(H_0 + V)\ket{\psi} = E\ket{\psi}. \tag{2.6}$$

Next, we expand our wavefunction in terms of the complete set of basis states in Eq. (2.3), where we have (unknown) coefficients c_m,

$$\ket{\psi} = \sum_{m=1}^{\infty} c_m \ket{\psi_m} \tag{2.7}$$

to obtain

$$\sum_{m=1}^{\infty} c_m(H_0 + V)\ket{\psi_m} = E\sum_{m=1}^{\infty} c_m \ket{\psi_m}. \tag{2.8}$$

8

Taking the inner product of Eq. (2.8) with the bra $\langle\psi_n|$ leads to

$$\sum_{m=1}^{\infty} H_{nm}c_m = Ec_n \tag{2.9}$$

where

$$
\begin{aligned}
H_{nm} &= \langle\psi_n|\,(H_0 + V)\,|\psi_m\rangle \\
&= \delta_{nm}E_n^{(0)} + H_{nm}^V
\end{aligned}
\tag{2.10}
$$

and

$$
\begin{aligned}
H_{nm}^V &= \langle\psi_n|\,V(x)\,|\psi_m\rangle \\
&= \frac{2}{a}\int_0^a \mathrm{d}x\,\sin\left(\frac{n\pi x}{a}\right)V(x)\sin\left(\frac{m\pi x}{a}\right).
\end{aligned}
\tag{2.11}
$$

We use the Kronecker delta δ_{nm} to signify elements on the main diagonal of our Hamiltonian matrix and $(1 - \delta_{nm})$ for the off-diagonal elements. This is because H_{nm}^V will typically take on different values on and off the main diagonal.

The problem is easily rendered into a convenient dimensionless form by using the infinite square well width a and ground state energy $E_1^{(0)}$:

$$\sum_{m=1}^{\infty} h_{nm}c_m = ec_n, \tag{2.12}$$

where $h_{nm} \equiv H_{nm}/E_1^{(0)}$ and $e \equiv E/E_1^{(0)}$. We will nearly always solve for systems in their dimensionless form since dealing with very small quantities like $\hbar$ and m_0 (small as compared to conventional units) introduces unnecessary numerical problems since, for example, $\hbar^2$ in SI units is on the order of 10^{-68} which is well below a typical machine epsilon.

2.1.2 Square Well With Periodic Boundary Conditions

As a next step, we use the same strategy, but instead of a box with infinite walls, we will use a "box" with periodic boundary conditions. Then the wave function satisfies the general periodicity condition:

$$\phi(x + a) = \phi(x), \tag{2.13}$$

with solutions that are the plane wave states,

$$\phi(x) \sim e^{ikx},\tag{2.14}$$

where $k^2 \equiv 2mE/\hbar^2$. Here, k can take on either positive or negative values. Imposition of the boundary conditions in Eq. (2.13) then requires

$$ka = 2n\pi,\tag{2.15}$$

where n is an integer: $n = \ldots, -2, -1, 0, 1, 2, \ldots$. The eigenvalues are

$$E_n = 4\left(\frac{n^2\pi^2\hbar^2}{2m_0a^2}\right) = 4n^2 E_1^{(0)}.\tag{2.16}$$

Note that these differ from the eigenvalues of an infinite square well:

  i. They have values that are four times as large for the same integer, n.

 ii. They are doubly degenerate (with one exception).

iii. $E = 0$ is possible, and also constitutes the one exception to point (ii).

The orthonormal basis states are then

$$\phi_n(x) = \sqrt{\frac{1}{a}}\exp\left[i\frac{2\pi n}{a}x\right],\tag{2.17}$$

where n is an integer.

2.1.3 Harmonic Oscillator

Does this plane-wave basis work? We recall the results from [8] for the case of the harmonic oscillator (which has well-known eigenvalues and wavefunctions) and compare this with the solution using periodic boundary conditions. This section can be considered a helpful illustration of the previous abstract outline of the methodology.

Infinite Square Well Basis

We place the harmonic oscillator potential inside an infinite square well defined in Eq. (2.1). The analytical form for this potential is

$$V_{\mathrm{HO}}(x) = \frac{1}{2}m_0\omega^2\left(x - \frac{a}{2}\right)^2 \qquad \text{for} \quad 0 < x < a,\tag{2.18}$$

10

and in dimensionless form we have

$$v_{\text{HO}}(x) = \frac{V_{\text{HO}}(x)}{E_1^{(0)}} = \frac{\pi^2}{4}\left(\frac{\hbar\omega}{E_1^{(0)}}\right)^2\left(\frac{x}{a}-\frac{1}{2}\right)^2 \tag{2.19}$$
$$= \left(\frac{\pi\gamma}{2}\right)^2\left(\frac{x}{a}-\frac{1}{2}\right)^2,$$

where we have defined $\gamma \equiv \hbar\omega/E_1^{(0)}$. Using this potential, the Hamiltonian matrix components in the basis (2.3) are, following Eq. (2.11),

$$H_{nm}^V = \langle\psi_n|V|\psi_m\rangle$$
$$= \frac{1}{a}\int_0^a dx\,\sin\left(\frac{n\pi x}{a}\right)\left[\frac{1}{2}m_0\omega^2\left(x-\frac{a}{2}\right)^2\right]\sin\left(\frac{m\pi x}{a}\right). \tag{2.20}$$

These integrals are relatively simple, and give (now dimensionless) matrix elements, where we now also include the kinetic energy contribution $n^2\delta_{nm}$, per Eq. (2.10).

$$h_{nm} = \frac{H_{nm}}{E_1^{(0)}} = \delta_{nm}\left[n^2 + \frac{\pi^2\gamma^2}{48}\left(1 - \frac{6}{(\pi n)^2}\right)\right] + (1-\delta_{nm})\gamma^2 g_{mn}, \tag{2.21}$$

where

$$g_{mn} = \frac{(-1)^{n+m}+1}{4}\left(\frac{1}{(n-m)^2} - \frac{1}{(n+m)^2}\right). \tag{2.22}$$

Periodic Boundary Conditions

For the case of periodic boundary conditions, we use Eq. (2.18) but now with the basis states in Eq. (2.17), so that the matrix elements are

$$H_{nm}^V = \langle\phi_n^{(0)}|V|\phi_m^{(0)}\rangle$$
$$= \frac{1}{a}\int_0^a dx\,e^{-i2\pi nx/a}\left[\frac{1}{2}m_0\omega^2\left(x-\frac{a}{2}\right)^2\right]e^{i2\pi mx/a}. \tag{2.23}$$

We can cast the integral into the dimensionless form

$$h_{nm}^V \equiv \frac{H_{nm}^V}{E_1^{(0)}} = \left(\frac{\pi\gamma}{2}\right)^2 I_{nm}, \tag{2.24}$$

where

$$I_{nm} = (-1)^{m-n}\int_{-1/2}^{1/2} u^2 e^{i2\pi(m-n)u}\,du. \tag{2.25}$$

This integral is straightforward, and when combined with the kinetic energy contribution, one obtains

$$h_{nm} = \delta_{nm}\left[4n^2 + \frac{\pi^2\gamma^2}{48}\right] + (1 - \delta_{nm})\left[\frac{\gamma^2}{8}\frac{1}{(m-n)^2}\right], \qquad (2.26)$$

which is clearly different from Eq. (2.21).

As in the infinite square well case we will have to truncate this matrix, so it makes sense to arrange the basis states in order of increasing energy. We will order the quantum numbers as $n = \{0, 1, -1, 2, -2, 3, -3, \ldots\}$, and then truncate at some $n_{\max}$. The transformation from the (computationally convenient) natural numbers to this sequence [21] can be performed with the function

$$n = \frac{1 + (-1)^k(2k-1)}{4} \qquad (2.27)$$

where k are the natural numbers. We will also label the quantum numbers with a new subscript n', where $n' = \{0, 1, 2, 3, 4, 5, 6, \ldots\}$ in the same order. So, for example, $n' = 4$ corresponds to $n = -2$.

Numerical Comparison of Square Well and Periodic Bases

We pause for a moment to compare the accuracy and efficiency of the two basis sets. In Fig. 2.1 we plot the numerical eigenenergies obtained for the two cases with $\gamma = 20$ and $n_{\max} = 60$. We use MATLAB's `eig` function [33], which determines the eigenvalues/vectors by putting the matrix in so-called Hessenberg form and then applying a QR decomposition recurrence scheme which converges to a so-called Schur decomposition form from which the final values are readily attainable [18, 19]. The two methods give very similar results, so an expansion in periodic boundary condition basis states is just as effective as the method used in [8]. In particular, either method reproduces the expected linear-in-n results to high accuracy for low-lying states, where the presence of the enclosing box is not noticed. This is the regime that is physically relevant to the harmonic oscillator potential. At higher values of n both cases produce energies that grow as n^2. This is when the wavefunction is sufficiently spread out (due to higher energies) that it appreciably "touches" the sides of the box, at which point the harmonic oscillator becomes a minor perturbation (contributing a constant v_{off} component) since we're now in the infinite square well regime.

We would also like to check convergence as a function of matrix size. To do this,
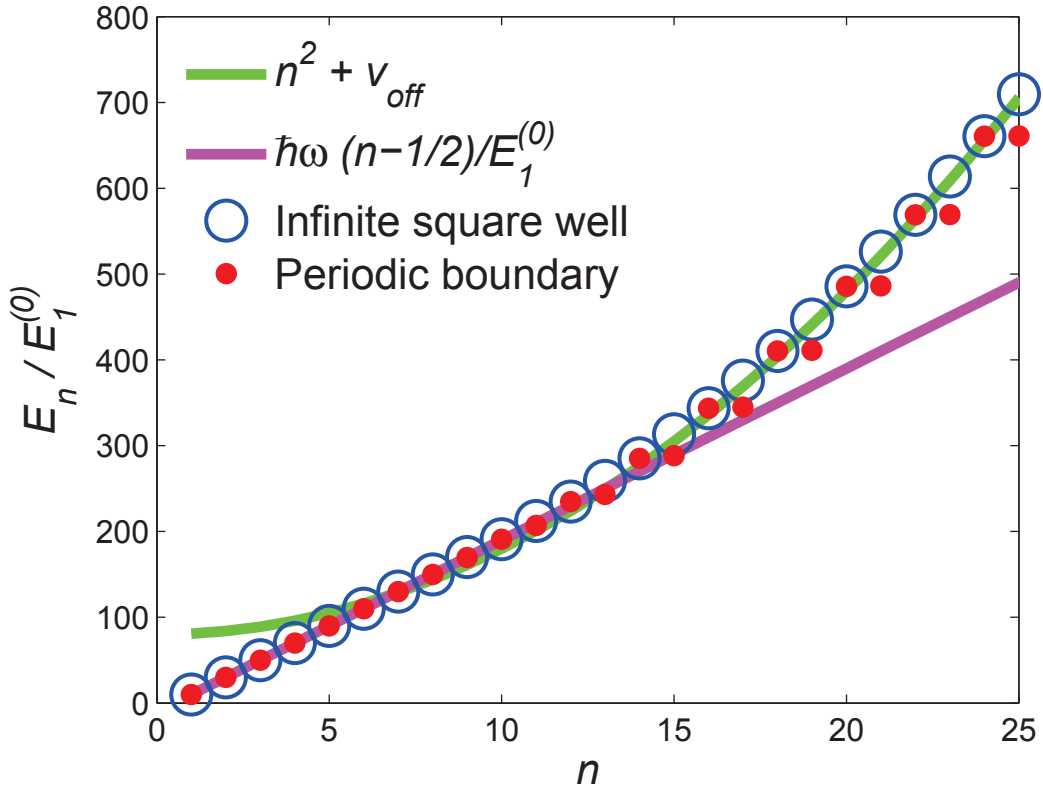
Figure 2.1: Plot of the normalized energy levels vs. quantum number n for numerical solutions using open (infinite square well) and periodic boundary conditions. We used $n_{\max} = 60$ and $\hbar\omega/E_1^{(0)} = 20$, and note that our quantum number n begins at unity (not zero, so here $n = n' + 1$). The rationale for the curve $n^2 + v_{\text{off}}$ is explained in [8]. Both results give the correct energy eigenvalues at low values of n, and both grow as n^2 at large values of n, reflecting the expected behaviour due to the confining box. Note the clear degeneracies at large n for the case with periodic boundary condition energies.

we compute the Fourier coefficients in our two basis sets of the harmonic oscillator ground state (of course any excited state would also do, but the integrals would become increasingly tedious to compute). Writing the analytical form of the ground state wavefunction using our usual dimensionless units gives

$$\psi_{\text{HO}}(x) = \left[\frac{\pi\gamma}{2a^2}\right]^{1/4} \exp\left[-\frac{\pi^2\gamma}{4a^2}\left(x - \frac{1}{2}\right)^2\right]. \tag{2.28}$$

We can compute the coefficients as

$$c_n = \langle \phi_n^{(0)} | \psi_{\mathrm{HO}} \rangle . \tag{2.29}$$
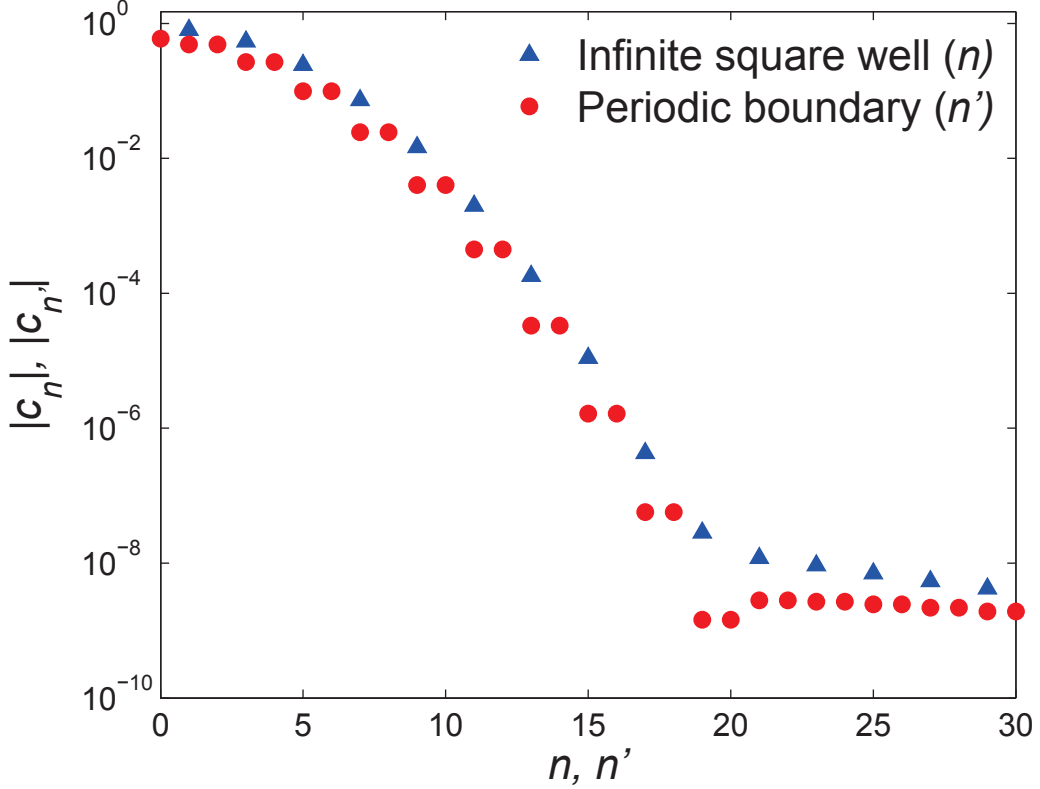
Figure 2.2: The numerically derived absolute values of the Fourier coefficients for the infinite square well and the periodic boundary condition embedding potentials, plotted on a semilog graph. The even cases for the infinite square well have finite nonzero results on the order of less than 10^{-15} and are not shown. Here, the truncated matrix dimension is $n_{\mathrm{max}} = 60$ and $\gamma = \hbar\omega/E_1^{(0)} = 20$. Analytical results cannot be distinguished from the numerical results. We see again that there is little computational difference between the periodic boundary conditions used in this paper and the method used in Ref. [8].

For the infinite square well, this gives[1]

$$c_n = \begin{cases} i^{(n-1)} \left(\frac{32}{\pi\gamma} \right)^{1/4} \exp\left[-n^2/\gamma \right] & n \text{ odd}, \\ 0 & n \text{ even}, \end{cases} \tag{2.30}$$

---

[1]See Ref. [8]. Note that this article has a typographical error in Eq. (15), which has been corrected here in Eq. (2.30).

where $n = 1, 2, 3, 4, \ldots$. This is actually an approximation; we take the integral bounds of Eq. (2.29) to be $(-\infty, \infty)$ rather than $(0, a)$ to avoid dealing with negligible error functions.

For the case of periodic boundary conditions, we can take the inner product with each eigenstate from Eq. (2.17). We obtain the coefficients

$$c_{n'} = (-1)^n \left(\frac{8}{\pi \gamma} \right)^{1/4} \exp \left[-4n^2/\gamma \right], \qquad (2.31)$$

which differ from those in Eq. (2.30). This difference is not significant, and shows that no real advantage for convergence can be gained by going to periodic boundary conditions. More importantly, no disadvantage occurs as well. Note that the coefficients are labeled by n' but the exponential is calculated with just n, using the correspondence described above.

To evaluate the efficiency we show the results for the coefficients on a log plot in Fig. 2.2; both methods yield similar results, with the smooth decay breaking down where $n \approx \hbar\omega/E_1^{(0)}$, which is the condition for the basis state energy equal to the crossover (from harmonic oscillator to square well) energy for the potential. Exact analytical results agree to seven digits in either case. Note that agreement can be systematically improved indefinitely in both cases by enlarging the width of the embedding square well. In practice this is achieved by increasing the value of γ (note the definition of γ immediately following Eq. (2.19), where it is clear that $\gamma \propto a^2$). However, for larger a we require a larger comparative n_{max} since the basis states will contain less high-frequency information (they are more spread out compared to the wavefunction). In any event this comparison for the ground state extends to other excited states, and shows that neither efficiency nor accuracy is compromised by adopting periodic boundary conditions.

2.2   Bloch's Theorem

Bloch's theorem [2] forms the foundation for dealing with periodic lattices, i.e., the physics of solids. Without it, solutions to the entire lattice would be completely computationally intractable. Because of its importance to everything that comes after, and because the proof is quite short and elegant, we recapitulate it here (adapted from [3]). We will restrict ourselves to one dimension for clarity, but the proof is readily generalized to two or three dimensions.

A periodic lattice is one that satisfies

$$V(x + a) = V(x) \tag{2.32}$$

for some "lattice constant" a. We now introduce a "translation operator" T_a for this lattice which operates as

$$T_a \psi(x) = \psi(x + a). \tag{2.33}$$

Lemma 2.2.1 *The translation operator T commutes with the Hamiltonian H.*

Proof:

$$T_a H(x)\psi(x) = H(x + a)\psi(x + a) = H(x)\psi(x + a) = H(x)T_a\psi(x) \tag{2.34}$$

since the Hamiltonian is translation invariant (no single unit cell has a special status). Therefore,

$$[T, H] = 0. \quad QED \tag{2.35}$$

Because they commute, they share the same eigenstates. So we have

$$T_a \psi(x) = \lambda(a)\psi(x) \tag{2.36}$$

for some complex number λ.

Theorem 2.2.2 (Bloch's Theorem) *For periodic potentials as in Eq. (2.32), the eigenstates satisfy*

$$\psi(x + a) = e^{iKa}\psi(x) \tag{2.37}$$

for a constant K.

Proof: Consecutive applications of the translation operator are additive.

$$T_a T_a \psi(x) = T_a \lambda(a)\psi(x) = \lambda(a)T_a\psi(x) = \lambda(a)\lambda(a)\psi(x) \tag{2.38}$$

but

$$T_a T_a \psi(x) = T_{a+a}\psi(x) = T_{2a}\psi(x) = \lambda(2a)\psi(x). \tag{2.39}$$

This can be done repeatedly; n applications of T_a (where n is some whole number) will give

$$\lambda(a)\lambda(a) \ldots n \text{ times} \ldots \lambda(a) = \lambda(na). \tag{2.40}$$

16

Such an eigenvalue can therefore be written as a complex exponential e^{iKa} where K is some constant (not dependent on position). *QED*

It can be further shown that K is real (see for example [3]) and takes on as many values as there are unit cells in the lattice. We will be treating lattices as mathematically infinite in extent (permissible since the infinity is in an extensive magnitude as opposed to an intensive magnitude; see [20] for a lucid modern treatment of which infinities are allowable or forbidden) so K will be treated as continuous.

The lattice constant a is in practice our unit cell length, and it should be clear that $-\pi < Ka < \pi$. In keeping with our emphasis on using dimensionless parameters, we will be treating the product $Ka/\pi \in (-1,1)$ as a single entity.

2.3   Kronig-Penney Model

The Kronig-Penney model [1] is constructed from a unit cell of width a consisting of a well of width b with height $V(x) = 0$ and barriers of width $a - b$ with height $V(x) = V_0$. Outside of the unit cell, the potential repeats such that $V(x+na) = V(x)$ for some integer n as shown in Fig. 2.3.
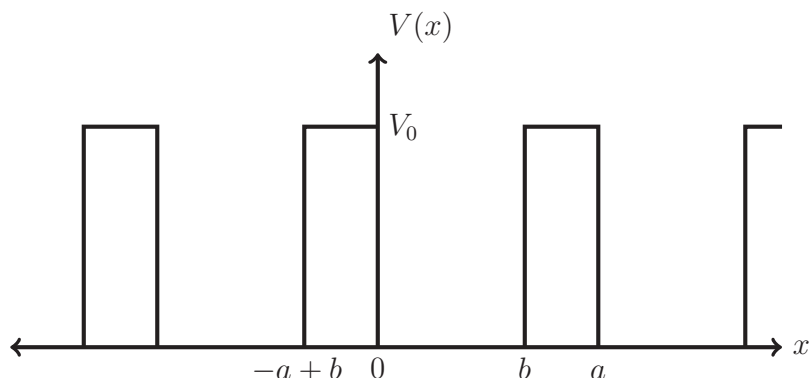
Figure 2.3: Representation of the Kronig-Penney model.

For states whose energies are below the barrier height one can solve the Schrödinger equation for each region in turn: a linear combination of two plane waves in the "well" regions

$$\psi_{\mathrm{I}}(x) = Ae^{ikx} + Be^{-ikx}, \tag{2.41}$$

where $k_1 = \sqrt{2mE/\hbar^2}$, followed by a linear combination of an exponentially decaying and an exponentially growing solution in the "barrier" regions

$$\psi_{\mathrm{II}}(x + b) = Ce^{\kappa_2 x} + De^{-\kappa_2 x} \tag{2.42}$$

17

where $\kappa_2 = \sqrt{2m(V_0 - E)/\hbar^2}$. Matching the wave functions and their derivatives at one interface determines two of the unknown coefficients. At the next interface a similar procedure determines two more coefficients, but this still leaves two unknown coefficients, from the next well section

$$\psi_{\text{III}}(x + a) = Ee^{ikx} + Fe^{-ikx} \tag{2.43}$$

and on this would go *ad infinitum*. Bloch's theorem (Eq. (2.37)) allows the second matching process to terminate the procedure, since

$$\psi_{\text{III}}(x + a) = e^{iKa}\psi_{\text{I}}(x). \tag{2.44}$$

Thus, we are left with four homogeneous equations with four unknowns. Since the determinant of the coefficients of these four equations must be zero for there to be a solution, one can derive the expression

$$\begin{aligned}
\cos{(Ka)} &= \cos{(k_1 b)}\cosh{[\kappa_2(a - b)]} \\
&+ \frac{\kappa_2^2 - k_1^2}{2k_1\kappa_2}\sin{(k_1 b)}\sinh{[\kappa_2(a - b)]}.
\end{aligned} \tag{2.45}$$

Equation (2.45) is thus an implicit equation for $E(K)$. In practice, one first selects a value of E; the absolute value of the right-hand-side of Eq. (2.45) is evaluated, and is either greater or less than unity (because of the cosine on the left-hand-side); if it is greater then there is no solution and these states are thus forbidden, while if it is less, then taking the inverse cosine of this quantity gives the value of Ka for which this energy is the solution.

One thus obtains alternating series of allowed solutions (energy bands) and forbidden solutions (band gaps). In the next chapter we will show plots of these solutions, comparing them to the output of our numerical procedure.

Chapter 3

One-Dimensional Potentials

In Chapter 2 we developed a matrix mechanics approach for an embedding potential that satisfies periodic boundary conditions. On its own this is of limited interest, as it doesn't offer much new over the original treatment [8] using an infinite square well embedding potential. In this chapter, we extend the approach using Bloch's theorem which enables us to explore the electronic band structure of arbitrary periodic potentials in one dimension. One particularly interesting feature of these different potentials we can explore are their effective electron and hole masses. We also examine the extent to which this approach agrees with the tight binding limit, both numerically and analytically, for large barriers.

3.1 Formalism

The formalism of Section 2.1 was developed for a wavefunction that satisfied the general periodicity condition

$$\phi(x + a) = \phi(x). \tag{3.1}$$

But in Section 2.2 we showed that a periodic lattice has unit cell boundary conditions

$$\psi(x + a) = e^{iKa}\psi(x). \tag{3.2}$$

The question then becomes: can we transition from the matrix mechanics method developed for Eq. (3.1) to satisfy the boundary condition of Eq. (3.2) straightforwardly? Because the basis states for Eq. (3.1) are plane waves i.e., complex exponentials, and the contribution from Bloch's theorem is a complex exponential, that perhaps all we need do is add the exponents. Recall Eq. (2.15), and now add to it the real factor

of the Bloch parameter

$$ka = 2n\pi \quad \rightarrow \quad ka = 2\pi n + Ka \tag{3.3}$$

where as before $k^2 = 2m_0 E/\hbar^2$. Hence the basis function energies become

$$
\begin{aligned}
E_n^{(0)} &= \frac{\hbar^2 \pi^2}{2m_0 a^2} \left(2n + \frac{Ka}{\pi} \right)^2 \\
&= E_1^{(0)} \left(2n + \frac{Ka}{\pi} \right)^2 .
\end{aligned}
\tag{3.4}
$$

Crucially, Eq. (3.4) modifies only the diagonal elements of the Hamiltonian. The off-diagonal elements are unaffected, because the basis states (2.17) are modified as

$$\phi_n^{(0)}(x) \rightarrow \frac{1}{\sqrt{a}} \exp\left[i \frac{2\pi n + Ka}{a} x \right] = e^{iKx} \phi_n^{(0)}(x). \tag{3.5}$$

But this means that $\phi_n^*(x) \rightarrow e^{-iKx} \phi_n^*(x)$. Thus the extra exponentials arising from the Bloch condition cancel one another in the matrix elements H_{nm}^V, since

$$H_{nm}^V = \frac{1}{a} \int_0^a dx\, e^{-iKx} e^{-i2\pi nx/a} V(x)\, e^{i2\pi mx/a} e^{+iKx} \tag{3.6}$$

and so the off-diagonal elements remain purely potential-dependent.

Our procedure then is as follows:

1. Solve for the (dimensionless) Hamiltonian matrix elements h_{nm}.

2. Populate and truncate a matrix containing elements h_{nm} and the (dimensionless) kinetic energy terms $4n^2 = (2n)^2$ along the main diagonal

$$
h_{nm} = \frac{H_{nm}}{E_1^{(0)}} =
\begin{pmatrix}
(2 \cdot 0)^2 + h_{00}^V & h_{01}^V & h_{02}^V & \cdots \\
h_{10}^V & (2 \cdot 1)^2 + h_{11}^V & h_{12}^V & \cdots \\
h_{20}^V & h_{21}^V & (2 \cdot 2)^2 + h_{22}^V & \cdots \\
\vdots & \vdots & \vdots & \ddots
\end{pmatrix}
$$

(note here for clarity we have written down $n, m = 0, 1, 2, \ldots$. In actual fact the indices are integers and can take on negative values, so properly they should go as $(0,0), (0,1), (0,-1), (1,0), (-1,0), (1,1), (1,-1), (-1,1), (-1,-1), (2,0)$ and so on.)

3. Make copies of the above matrix and repeatedly seed to the main diagonal values of $Ka/\pi \in (-1, 1)$.

$$
h_{nm} = \begin{pmatrix}
(0 + Ka/\pi)^2 + h_{00}^V & h_{01}^V & h_{02}^V & \cdots \\
h_{10}^V & (2 + Ka/\pi)^2 + h_{11}^V & h_{12}^V & \cdots \\
h_{20}^V & h_{21} & (4 + Ka/\pi)^2 + h_{22}^V & \cdots \\
\vdots & \vdots & \vdots & \ddots
\end{pmatrix}
$$

Each matrix is then diagonalized separately yielding a column of eigenenergies. That is, one populates the matrix for the unit cell *once* and then repeatedly diagonalizes for different values of Ka/π, thus "sweeping out" the energy spectrum.

3.2 Matrix Method for the Kronig-Penney Model

We are now in a position to apply this procedure to the Kronig-Penney model. As outlined in the procedure of the previous section, we begin by calculating the dimensionless Hamiltonian matrix elements h_{nm} for a unit cell.

Rather than previously where we defined the potential inside the unit cell as

$$
V(x) = \begin{cases}
0 & 0 < x < b \\
V_0 & b < x < a,
\end{cases}
\tag{3.7}
$$

we find it convenient to shift the unit cell so that the well is centrally-located such that the unit cell becomes symmetric, as

$$
V(x) = \begin{cases}
V_0 & 0 < x < \frac{a-b}{2} \\
0 & \frac{a-b}{2} < x < \frac{a+b}{2} \\
V_0 & \frac{a+b}{2} < x < a.
\end{cases}
\tag{3.8}
$$

A representation of this potential is shown in Fig. 3.1.

We now employ Eq. (2.23) but with our new potential to get

$$
H_{nm}^V = \frac{1}{a} \int_0^a \mathrm{d}x \, e^{-i2\pi n x/a} \, V(x) \, e^{i2\pi m x/a}.
\tag{3.9}
$$

Now defining $v_0 \equiv V_0/E_1^{(0)}$ and making the substitution $x' = x/a$ and thereafter
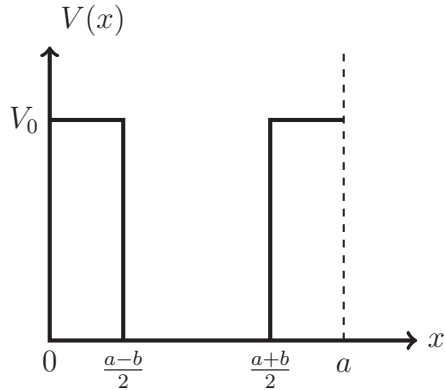
Figure 3.1: Centralized version of the Kronig-Penney unit cell.

dropping the dummy prime we get

$$h_{nm}^V = v_0 \left(\int_0^{(a-b)/2} + \int_{(a+b)/2}^a \right) \mathrm{d}x \, e^{i2\pi(m-n)x}. \tag{3.10}$$

This integral is elementary and yields, after making the substitution $\rho \equiv b/a$ i.e., the fraction of the unit cell that's occupied by the well,

$$
\begin{aligned}
h_{nm} = \; & \delta_{nm} \left[(2n)^2 + v_0(1-\rho) \right] \\
& + (1 - \delta_{nm}) v_0 \frac{(-1)^{m-n+1}}{\pi} \frac{\sin\left[\pi(m-n)\rho\right]}{m-n}
\end{aligned} \tag{3.11}
$$

where we have included the main diagonal kinetic energy components. Note that the main-diagonal component h_{nn}^V is the "area" of the barrier. Now we introduce the Bloch terms to finally give

$$
\begin{aligned}
h_{nm} = \; & \delta_{nm} \left[\left(2n + \frac{Ka}{\pi}\right)^2 + v_0(1-\rho) \right] \\
& + (1 - \delta_{nm}) v_0 \frac{(-1)^{m-n+1}}{\pi} \frac{\sin\left[\pi(m-n)\rho\right]}{m-n}.
\end{aligned} \tag{3.12}
$$

Now, continuing with the procedure of the previous section, we choose some matrix truncation size $n_{\max}$ (equivalent to choosing an finite set of basis states), a (dimensionless) value of the barrier height v_0, and then repeatedly diagonalize the matrix for different values of $Ka/\pi \in (-1, 1)$. For $v_0 = 0$ we show the results in Fig. 3.2a. We then introduce barriers of height $v_0 = 10$ and again form a plot, shown in Fig. 3.2b. Moreover, we overlay the known analytical solutions to the Kronig-Penney model

22
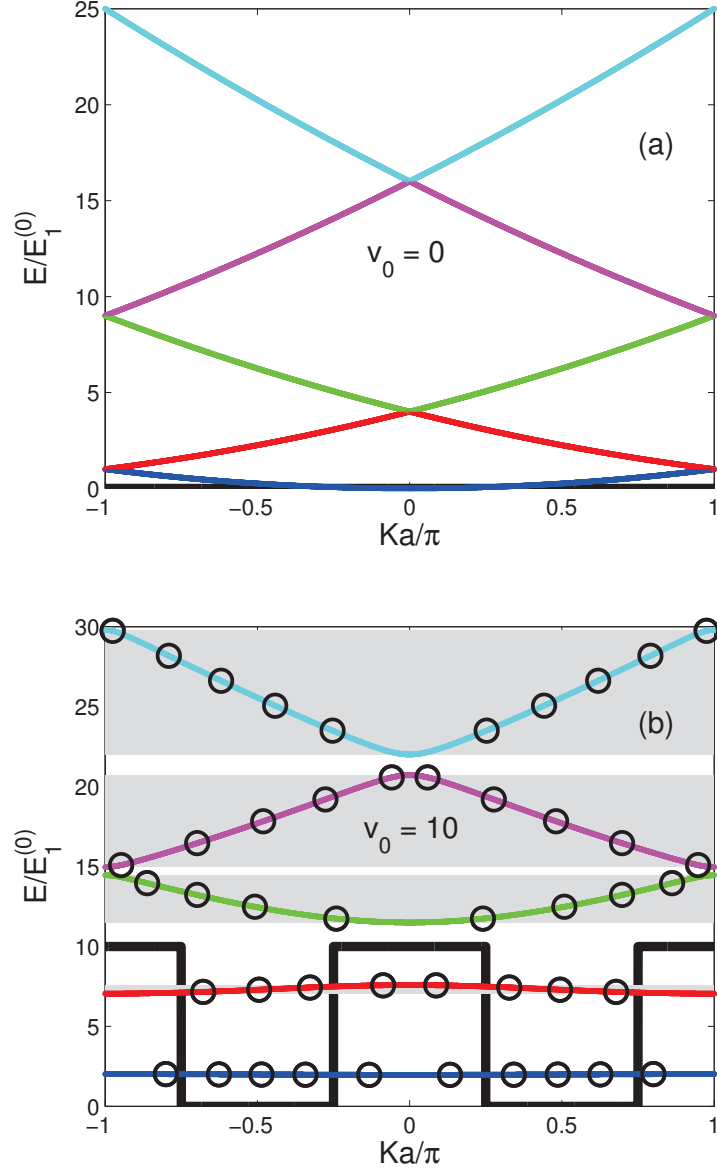
Figure 3.2: Solutions to the Kronig-Penney potential with (a) no well/barrier, and (b) a repeated well/barrier sequence with barrier height $v_0 = 10$. In (b) we have also indicated with open circles some of the analytical solutions to Eq. (2.45). A schematic representation of the potential (as a function of x, with an arbitrary horizontal scale) is shown to indicate the boundedness of the energy bands. The matrix solutions use $n_{\max} = 60$, and we have used $\rho = b/a = 0.5$. Note that K can be varied continuously—there are no finite-size effects. We write K in terms of π/a, so the boundaries in the plot are at ± 1. For the purposes of plotting we used 1601 values of Ka/π for each band, which takes just a few seconds to run, including plotting, on an Intel 2500K processor. Readers may recognize $K = \pm\pi/a$ as the boundaries of the first Brillouin zone. Note that we have lightly shaded the bands of energies where states exist. The shading is not visible behind the lowest band in the figure, because it hardly disperses.

23

from Eq. (2.45).

Recall that each diagonalization for a particular value of Ka/π, a column of eigenenergies is produced. We have indicated these separate entries in the column by different colours, which in one-dimension correspond nicely with the physical solutions. In higher dimensions, however, these colours may not have physical significance (most band diagrams in the literature just use black for every band).

We can see that for the case of $v_0 = 0$, we recapitulate the folded free electron, plane-wave parabolic energy bands. As we turn on the periodic potential (e.g., with $v_0 = 10$) we see band gaps emerge, with larger gaps in the lower-energy bands, and more curvature (i.e., band width) in the upper bands. Note the band gaps also form well above the potential barriers.[2] The analytical solutions from Eq. (2.45) are in complete agreement. We have thus succeeded in demonstrating that this numerical method works for periodic arrays. The familiar result of energy bands separated by gaps with no states, owing to the limited overlap of neighbouring wells, is now apparent from both a (familiar) analytical and a (less familiar) numerical point of view.

3.3   Tight Binding

Our solution manifestly reproduces the free electron limit, as shown in Fig. 3.2a. For larger barriers (deeper wells), we expect to approach the limit of the tight binding model. A full review of tight binding is beyond the scope of this monograph, and we will simply cite the known results to compare with (standard texts like [5] will provide the details).

Including a scalar term E_0 that does not depend on the reciprocal lattice vector K, in one dimension the tight-binding model is given by

$$E(K) = E_0 - \sum_n t_n e^{i\mathbf{K}\cdot\boldsymbol{\delta}_n} \tag{3.13}$$

where $\boldsymbol{\delta}_n = \pm na\hat{x}$ with $\hat{x}$ being the unit vector along the single-dimensional axis with a being the lattice constant, n is a whole number, and $\mathbf{K} = K\hat{x}$. The hopping integrals t_n are a measure of the overlap between the wavefunctions of different wells, and thus represent the probability amplitude of the electron tunneling from one well to another. Since the terms of the sum can be reduced to $t_n \left(e^{iKna} + e^{-iKna} \right)$ for each

---

[2]Marsiglio has colourfully expressed this as "a jet airliner feeling a cobblestone path far below it."

Table 3.1: Linear regression coefficients of determination (R^2) for tight binding fits to the Kronig-Penney model, for nearest-neighbour (nn), next-nearest-neighbour (nnn), and next-next-nearest-neighbour.

v_0	nn	nnn	nnnn
0	0.9231	0.9812	0.9928
1	0.9644	0.9964	0.9995
3	0.9940	0.9999	1.0000
10	1.0000	1.0000	1.0000

particular n, this becomes

$$E(K) = E_0 - 2t_1 \cos(Ka) - 2t_2 \cos(2Ka) - 2t_3 \cos(3Ka) - \ldots \tag{3.14}$$

with each nth-nearest-neighbour contributing a $-2t_n \cos(nKa)$ term. In typical introductory treatments only the nearest-neighbour (nn) model is considered with perhaps the next-nearest-neighbour (nnn) contribution given as a homework exercise. Given that the electron wavefunctions are exponentially-decaying in the barriers and that further than next-nearest neighbour contributions have to tunnel through multiple barriers, it should be clear that $|t_1| \ll |t_2| \ll |t_3| \ll \ldots$, justifying the approximations.

Our method of course makes no mention of some finite amount of nearest-neighbour contributions but rather considers the entire extended lattice all at once through Bloch's theorem. Thus we can compare with tight-binding in two ways: the depth of the well (the deeper the well the better the fit to tight-binding) and the number of nearest-neighbour contributions included in our tight-binding comparison.

We can make a numerical comparison of the functional form by performing a linear regression of our diagonalization with some function $E - 2t_1 \cos(x)$ where $x = Ka$. For next-nearest-neighbour we would use some function $E - 2t_1 \cos(x) - 2t_2 \cos(2x)$, etc. We use MATLAB's `fit` function [36] for this purpose.

In Fig. 3.3 we show some results comparing our matrix diagonalization with the nearest-neighbour tight-binding cosine. As the barrier height increases, the diagonalization approaches the expected limit, as evidenced both visually and through the R^2 linear regression coefficient of determination.

Further, in Table 3.1 we expand these results to next-nearest-neighbour (nnn) and next-next-nearest-neighbour (nnnn). As expected the fit is improved by including the contribution form farther wells, to the extent that even for no barriers at all next-next-nearest-neighbour has $R^2 > 0.99$.
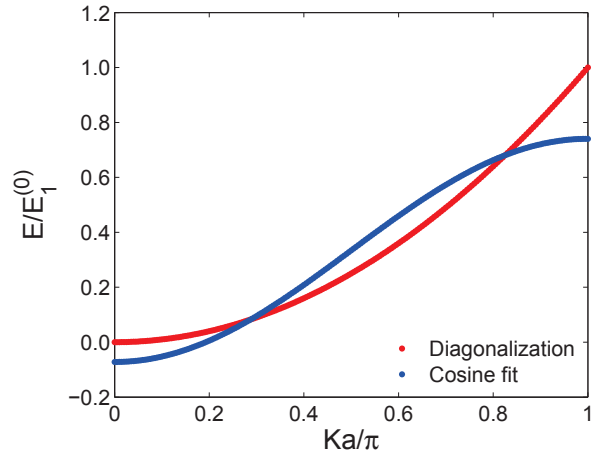
(a) $v_0 = 0, R^2 = 0.9231$
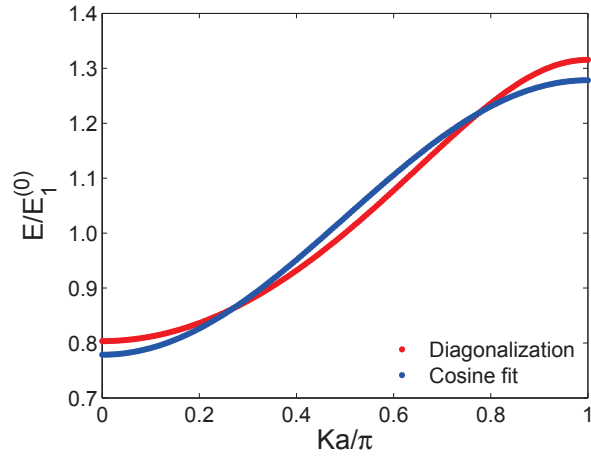
(b) $v_0 = 2, R^2 = 0.9856$
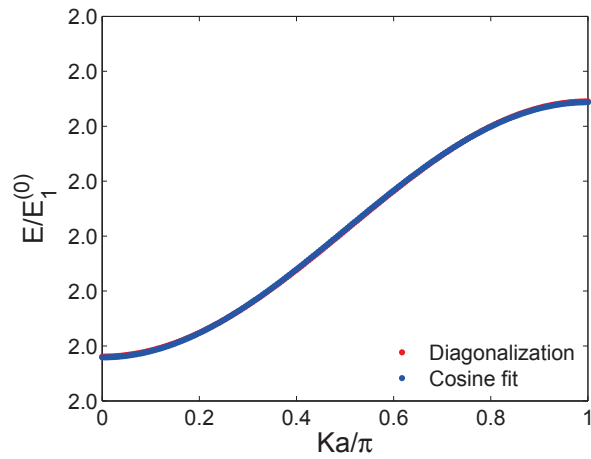
(c) $v_0 = 10, R^2 = 1.0000$

Figure 3.3: Nearest-neighbour tight binding results for the $\rho = 0.5$ Kronig-Penney model at various barrier heights.

Table 3.2: Best fit values of the hopping integrals t_i from linear regressions for tight binding fits to the Kronig-Penney model, for nearest-neighbour (nn), next-nearest-neighbour (nnn), and next-next-nearest-neighbour.

	nn	nnn		nnnn		
v_0	t_1	t_1	t_2	t_1	t_2	t_3
0	0.2036	0.2036	-0.0513	0.2031	-0.0513	0.0230
1	0.1688	0.1688	-0.0308	0.1686	-0.0308	0.0095
3	0.0902	0.0902	-0.0070	0.0902	-0.0070	0.0009
10	0.0116	0.0116	-0.0001	0.0116	-0.0001	-1.4e-06

In Table 3.2 we show the best fit values for the hopping integrals t_i for nn, nnn, and nnnn models. As expected, larger barriers correspond to decreasing absolute values of the hopping integrals (since there's a lower probability of transition), and higher-order hopping integrals decrease at a faster rate.

Thus we can consider our method to be a useful tool for motivating and justifying the tight binding model. Students can see for themselves that turning on the barriers causes the energy band to morph into a cosine curve even for modest values of v_0. When the tight binding model proper is introduced, the mathematical results will then build on firmer intuitions.

3.3.1 Analytical Tight Binding Limit

So far we have merely investigated the tight binding limit by a numerical fitting, which would not necessarily give us back the "correct" values of t_1, t_2, etc., but we can do better. Refer back to Eq. (2.45),

$$
\begin{aligned}
\cos\left(Ka\right) &= \cos\left(k_1 b\right)\cosh\left[\kappa_2(a-b)\right] \\
&+ \frac{\kappa_2^2 - k_1^2}{2k_1\kappa_2}\sin\left(k_1 b\right)\sinh\left[\kappa_2(a-b)\right],
\end{aligned}
\tag{3.15}
$$

where $k_1 = \sqrt{2mE/\hbar^2}$ and $\kappa_2 = \sqrt{2m(V_0 - E)/\hbar^2}$. We can investigate the tight binding limit analytically by taking V_0 large, which permits us to make the approximations

$$
\begin{aligned}
\cosh\left[\kappa_2(a-b)\right] \\
\sinh\left[\kappa_2(a-b)\right]
\end{aligned}
\approx \frac{e^{\kappa_2(a-b)}}{2}.
\tag{3.16}
$$
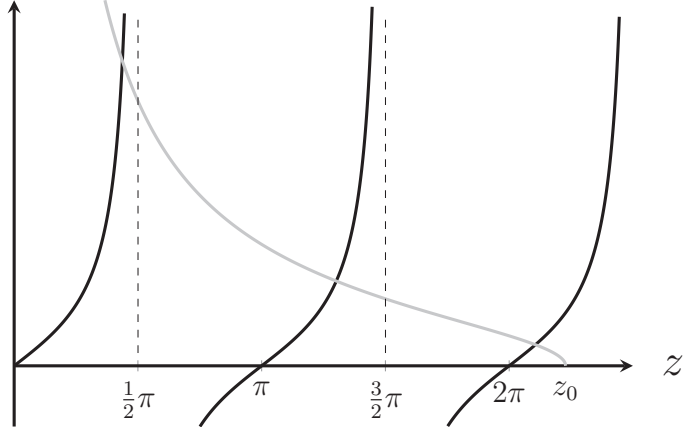
Figure 3.4: Graphical depiction of solutions to Eq. (3.19). The LHS is plotted in black and the RHS is plotted in grey. We can clearly see that the first solution for large z_0 is $z_1 \lesssim \pi/2$.

Then using the trigonometric identities $\cos k_1 b = \cos^2\left(\frac{k_1 b}{2}\right) - \sin^2\left(\frac{k_1 b}{2}\right)$ and $\sin k_1 b = 2\sin\left(\frac{k_1 b}{2}\right)\cos\left(\frac{k_1 b}{2}\right)$ we can write (after some algebraic manipulation)

$$\nu = \left(\cos\frac{k_1 b}{2} - \frac{k_1}{\kappa_2}\sin\frac{k_1 b}{2}\right)\left(\cos\frac{k_1 b}{2} + \frac{\kappa_2}{k_1}\sin\frac{k_1 b}{2}\right) \tag{3.17}$$

where $\nu = 2\,e^{-\kappa_2(a-b)}\cos(Ka)$. Taking the LHS to be zero (since the absolute value of the exponent is large), we can set the left-hand parenthesis on the RHS to zero corresponding to the lowest even state. That is

$$\cos\frac{k_1 b}{2} - \frac{k_1}{\kappa_2}\sin\frac{k_1 b}{2} = 0. \tag{3.18}$$

Further, we write $z = \frac{k_1 b}{2}$ and $z_0^2 - z^2 = \kappa_2^2\left(\frac{b}{2}\right)^2$ which leads us to write Eq. (3.18), after some algebra, as

$$\tan z = \sqrt{\left(\frac{z_0}{z}\right)^2 - 1}. \tag{3.19}$$

This transcendental equation must be solved numerically, and we can see graphically in Fig. 3.4 that there is a solution for $z \lesssim \pi/2$. This solution we call $z_1 = \alpha\frac{\pi}{2}$ where α is some parameter between 0 and 1.

The simplification in Eq. (3.18) is not entirely correct of course, since there is some non-zero coupling between neighbouring wells. We therefore introduce some coupling parameter δ_K which is exponentially small to get a solution $z = z_1 + \delta_K$.

28

Returning to Eq. (3.17) we can write it as

$$\nu = \left(\cos z - \frac{z}{\sqrt{z_0^2 - z^2}} \sin z \right) \left(\cos z + \frac{\sqrt{z_0^2 - z^2}}{z} \sin z \right). \tag{3.20}$$

We now make use of the trigonometric identities

$$\cos(z_1 + \delta_K) = \cos z_1 \cos \delta_K - \sin z_1 \sin \delta_K \approx \cos z_1 - \delta_K \sin z_1 \tag{3.21}$$

$$\sin(z_1 + \delta_K) = \sin z_1 \cos \delta_K + \cos z_1 \sin \delta_K \approx \sin z_1 + \delta_K \cos z_1 \tag{3.22}$$

and expand the left-hand parenthesis to first order in δ_K. Since the right-hand parenthesis is not small, we neglect the contributions from δ_K, giving, after dividing out a $\cos z_1$,

$$\cos z_1 \left(1 + \frac{\sqrt{z_0^2 - z_1^2}}{z_1} \tan z_1 \right) = \frac{1}{\sqrt{1 + \tan^2 z_1}} \left(1 + \frac{\sqrt{z_0^2 - z_1^2}}{z_1} \tan z_1 \right) \tag{3.23}$$

Now using Eq. (3.19) with $z \approx z_1$, this expression can be written purely in terms of z_0 and z_1 and after some algebraic manipulation reduces to the simple form z_0/z_1. Putting this in Eq. (3.20) and expanding the left-hand parenthesis with Eqs. (3.21) and (3.22) gives

$$
\begin{aligned}
\frac{z_1}{z_0}\nu &= \cos z_1 - \delta_K \sin \delta_K - \frac{(z_1 + \delta_K)}{\sqrt{(z_0^2 - z_1^2)\left(1 - \frac{z_1 \delta_K}{z_0^2 - z_1^2}\right)}} \sin z_1 + \delta_K \cos z_1 \\
&\approx \cancel{\cos z_1} - \delta_K \sin \delta_K - \frac{z_1}{\sqrt{z_0^2 - z_1^2}} \sin z_1 \left(\cancel{1} + \frac{\delta_K}{z_1} + \frac{\delta_K}{2} \frac{z_1}{z_0^2 - z_1^2} \right)(1 + \delta_K \cot z_1) \\
&= -\delta_K \cos z_1 \left\{ \frac{z_1}{\sqrt{z_0^2 - z_1^2}} + \tan z_1 \left(1 + \frac{1}{\sqrt{z_0^2 - z_1^2}} + \frac{1}{2} \frac{z_1^2}{(z_0^2 - z_1^2)^{\frac{3}{2}}} \right) \right\} \tag{3.24}
\end{aligned}
$$

where in the second line we canceled out the component that corresponded to Eq. (3.18) and in the third line we've neglected terms of order $\mathcal{O}(\delta_K^2)$. Now again writing $\cos z_1 = (1 + \tan^2 z_1)^{-\frac{1}{2}}$ and using Eq. (3.19) with $z \approx z_1$ this expression can be simplified to

$$\frac{z_1}{z_0}\nu = -\delta_K \frac{z_1}{z_0} \left\{ \frac{3}{2} \frac{z_1}{z_0^2 - z_1^2} + \frac{1}{z_1} \left(1 + \sqrt{z_0^2 - z_1^2} \right) \right\} \tag{3.25}$$

or finally

$$\delta_K = \frac{-\nu}{\frac{3}{2}\frac{z_1}{z_0^2 - z_1^2} + \frac{1}{z_1}\left(1 + \sqrt{z_0^2 - z_1^2}\right)} \tag{3.26}$$

where again z_1 is determined numerically and

$$z_0^2 = z^2 + \kappa_2^2\left(\frac{b}{2}\right)^2 = \left(\kappa_2^2 + k_1^2\right)\left(\frac{b}{2}\right)^2 = \left(\frac{\pi}{2}\right)^2\frac{V_0}{E_1} \tag{3.27}$$

where we have introduced $E_1 = \pi^2\hbar^2/(2m_0 b^2) = E_1^{(0)}(b/a)^2 = E_1^{(0)}\rho^2$. Now since $z = z_1 + \delta_K$, dropping terms of order $\mathcal{O}(\delta_K^2)$ we have

$$z^2 = \frac{2m_0 E}{\hbar^2}\left(\frac{b}{2}\right)^2 = z_1^2 + 2z_1\delta_K \tag{3.28}$$

or

$$E = \frac{4\hbar^2}{2m_0 b^2}\left(\alpha^2\left(\frac{\pi}{2}\right)^2 + 2\alpha\frac{\pi}{2}\delta_K\right). \tag{3.29}$$

Finally,

$$\frac{E}{E_1} = \frac{E}{E_1^{(0)}}\frac{1}{\rho^2} = \alpha^2 - \frac{\frac{8\alpha}{\pi}e^{-2\left(\frac{a}{b}-1\right)\sqrt{z_0^2 - z_1^2}}}{\frac{3}{2}\frac{z_1}{z_0^2 - z_1^2} + \frac{1}{z_1}\left(1 + \sqrt{z_0^2 - z_1^2}\right)}\cos\left(Ka\right) \tag{3.30}$$

which has the functional form of nearest-neighbour tight binding (see Eq. (3.14), with t_1 now given an explicit analytical form in Eq. (3.30)).

Unlike before where we were merely checking if our diagonalizations could be fit to a tight binding functional form, now with Eq. (3.30) we have an entirely independent calculation of the lowest energy band.

We show some results for the $\rho = 0.5$ Kronig-Penney model at various barrier heights in Fig. 3.5. The agreement between our analytical limit and our diagonalization procedure is excellent; for $v_0 = 70$ as an example the (dimensionless) discrepancy is on the order of 10^{-7}.

3.4 General Potential Shapes

We now have the freedom to study periodic arrays of potentials with any shape, simply by performing many matrix diagonalizations (corresponding to different values of Ka) for the wave function in one unit cell. Figure 3.6 shows various examples of periodic potentials that we will consider here.

We chose these potentials since they represent a reasonable gamut of potential

(a) $v_0 = 3$, $\alpha = 0.556$

(b) $v_0 = 10$, $\alpha = 0.706$

(c) $v_0 = 30$, $\alpha = 0.809$

(d) $v_0 = 50$, $\alpha = 0.846$

(e) $v_0 = 70$, $\alpha = 0.867$

(f) $v_0 = 100$, $\alpha = 0.887$
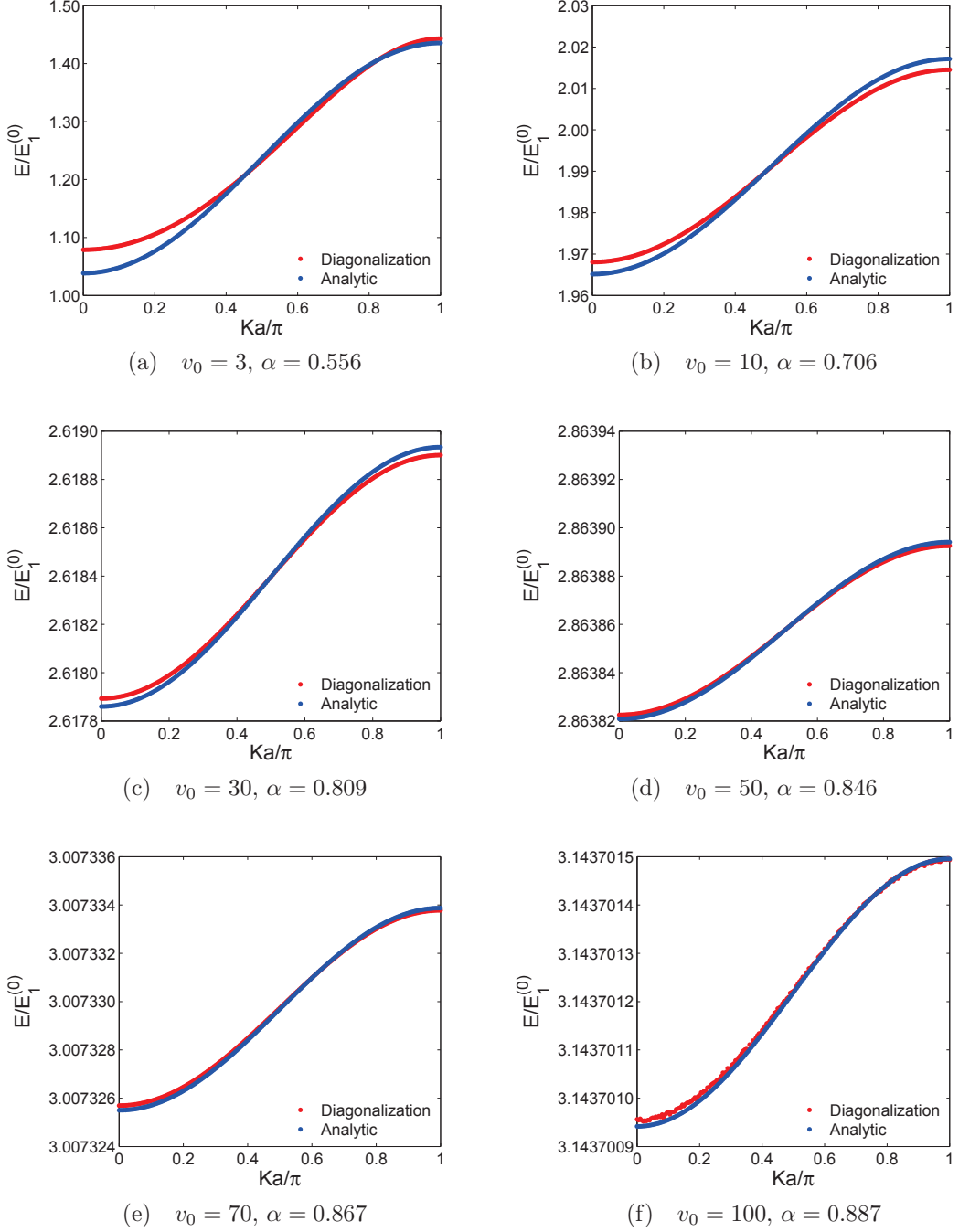
Figure 3.5: Comparisons between our diagonalization routine and the analytical solution of the tight binding limit for the Kronig-Penney model from Eq. (3.30), with $\rho = 0.5$. Note the change in the number of significant digits along the vertical axis.
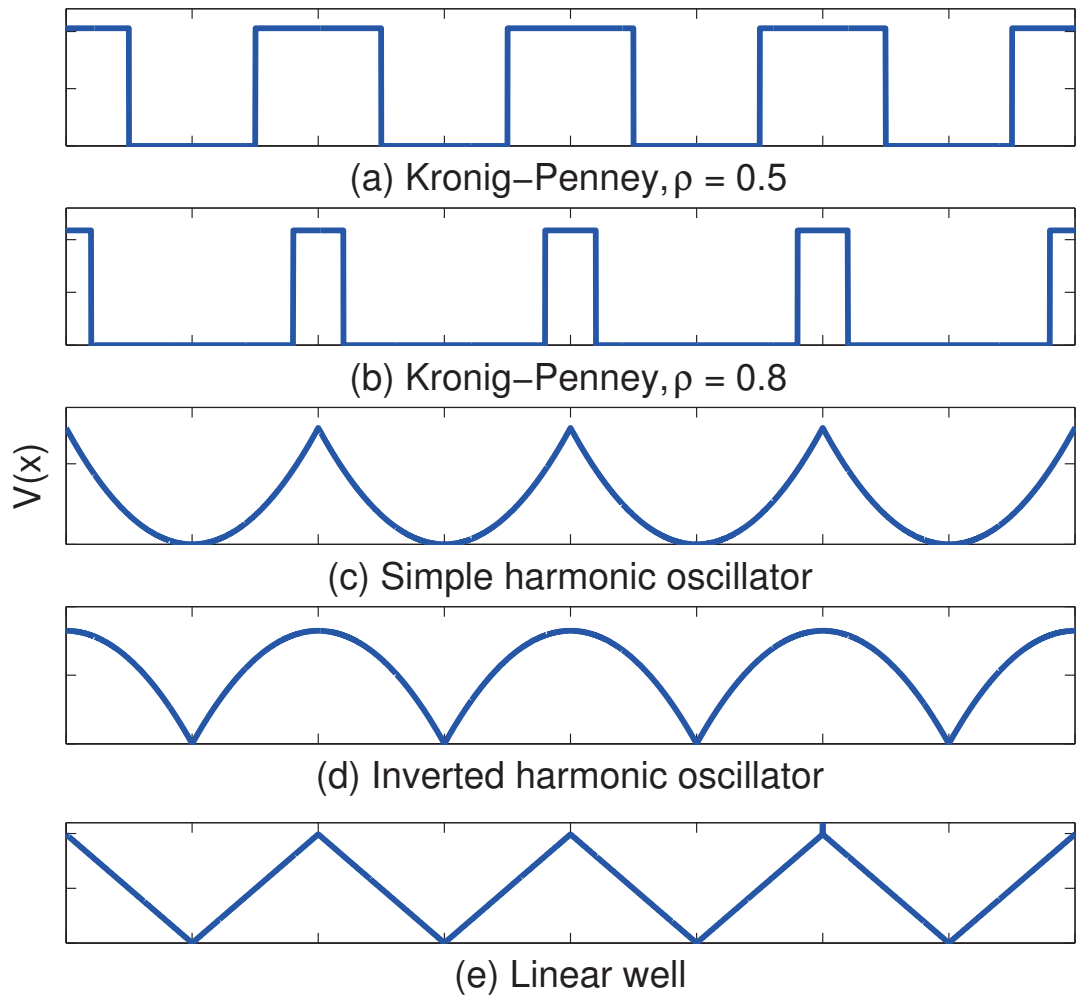
Figure 3.6: Schematic representations of the potentials used for comparing energy band structures.

shapes, in particular the cusps at the peaks of the barriers. Further, we can obtain analytical solutions for their matrix elements.

The reader might rightly ask, "Since we're performing matrix mechanics numerically anyway, why do we bother computing these matrix elements analytically? Why not just perform the integration numerically and be done with it?" Some responses:

- *Computational efficiency.* Analytic expressions can typically be evaluated much faster than numerical integrations, since our particular implementation involves rapidly oscillating basis states for larger matrices.

- *Mathematical insight.* Numerical results are black boxes, whereas analytic expressions may suggest new interpretations of the problem.

- *Numerical error.* Analytic expressions can avoid errors introduced from numerical procedures; for example, integrating over sharply changing features like walls or cusps.

- *Pedagogy.* The calculation of the analytic expressions can be a useful exercise in understanding the matrix mechanics methodology.

- *It's fun.* Computing integrals is its own reward [24].

We have already explored the matrix elements for the Kronig-Penney model, with matrix elements given by Eq. (3.12). We explore two versions: one with even amounts of wells and barriers i.e., $\rho = 0.5$, and one with thinner barriers i.e., $\rho = 0.8$ (see Figs. 3.6a, b respectively).

For the harmonic oscillator (see Fig. 3.6c), beginning with Eq. (2.23), we can cast the integral into the dimensionless form (recall that $\gamma \equiv \hbar\omega/E_1^{(0)}$)

$$h_{nm}^V \equiv \frac{H_{nm}^V}{E_1^{(0)}} = \left(\frac{\pi\gamma}{2}\right)^2 I_{nm}, \tag{3.31}$$

where

$$I_{nm} = (-1)^{m-n} \int_{-1/2}^{1/2} u^2 e^{i2\pi(m-n)u} \, \mathrm{d}u. \tag{3.32}$$

This integral is elementary, and the required dimensionless matrix elements with the main diagonal Bloch contributions are

$$h_{nm} = \delta_{nm} \left[\left(2n + \frac{Ka}{\pi}\right)^2 + \frac{\pi^2\gamma^2}{48}\right] + (1 - \delta_{nm}) \left[\frac{\gamma^2}{8} \frac{1}{(m-n)^2}\right]. \tag{3.33}$$

For the inverted harmonic oscillator potential (see Fig. 3.6d) we use

$$V(x) = \begin{cases} -\frac{1}{2}m\omega^2 \left[x^2 - \frac{a^2}{4} \right] & 0 < x < \frac{a}{2}, \\ -\frac{1}{2}m\omega^2 \left[(x-a)^2 - \frac{a^2}{4} \right] & \frac{a}{2} < x < a. \end{cases} \qquad (3.34)$$

This system has matrix elements

$$h_{nm} = \delta_{nm} \left[\left(2n + \frac{Ka}{\pi} \right)^2 + \frac{\pi^2\gamma^2}{24} \right] - (1 - \delta_{nm}) \left[\frac{\gamma^2}{8} \frac{(-1)^{m-n}}{(m-n)^2} \right]. \qquad (3.35)$$

Note the difference between the above equation and Eq. (3.33) in both the off-diagonal elements (change of sign) and the diagonal elements (factor of 2 in the potential term).

A third example is the linear well (see Fig. 3.6e), with a potential defined by

$$V(x) = \begin{cases} 2A \left(\frac{1}{2} - \frac{x}{a} \right) & 0 < x < \frac{a}{2}, \\ 2A \left(\frac{x}{a} - \frac{1}{2} \right) & \frac{a}{2} < x < a. \end{cases} \qquad (3.36)$$

This system has matrix elements

$$\begin{aligned} h_{nm} = \ & \delta_{nm} \left[\left(2n + \frac{Ka}{\pi} \right)^2 + \frac{A}{2} \right] \\ & - (1 - \delta_{nm}) \frac{A}{\pi^2(m-n)^2} \left[1 - (-1)^{m-n} \right]. \end{aligned} \qquad (3.37)$$

Of course, the method is general and can be applied to periodic arrays that have no analytical solutions. Students can explore whatever (integrable) potential they choose.

3.4.1 Comparing Band Structures

Results for the band structures corresponding to the potential shapes in Fig. 3.6 are shown in Figs. 3.7, 3.8, 3.9, 3.10, and 3.11. We chose parameters such that in all cases three bands with energies less than the maximum barrier height would form, and in which the third band would have an energy difference between the highest level (at $Ka = \pm\pi$) and the maximum barrier potential, $V_{\max}$, of $\Delta E = E_1^{(0)}$.

As mentioned earlier, bands with gaps form at energies above the barrier maxima as well. However, the character of these bands is strongly dependent on the type of periodic potential used. In particular, for the last three potentials the gap can be
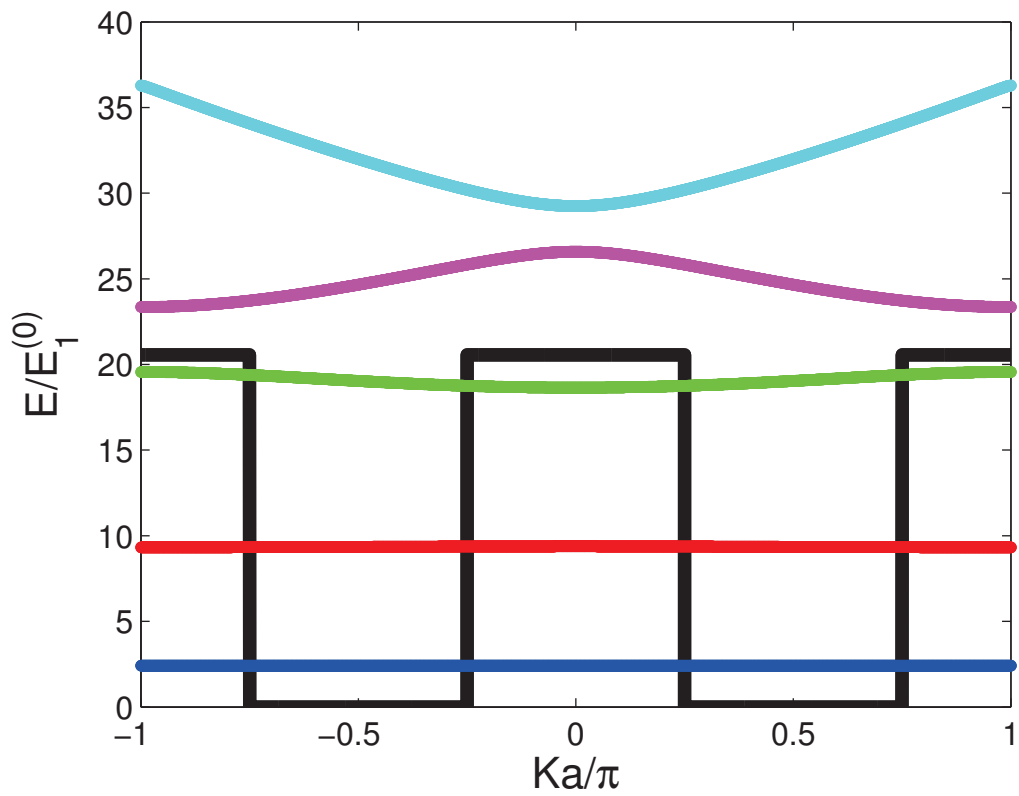
Figure 3.7: Energy band diagram for the Kronig-Penney potential with $\rho = 0.5$ and $v_0 = 20.5607$ (shown here schematically and also in Fig. 3.6a). Note the presence of energy gaps for the high-energy bands. These gaps persist with diminishing size as the energy increases.
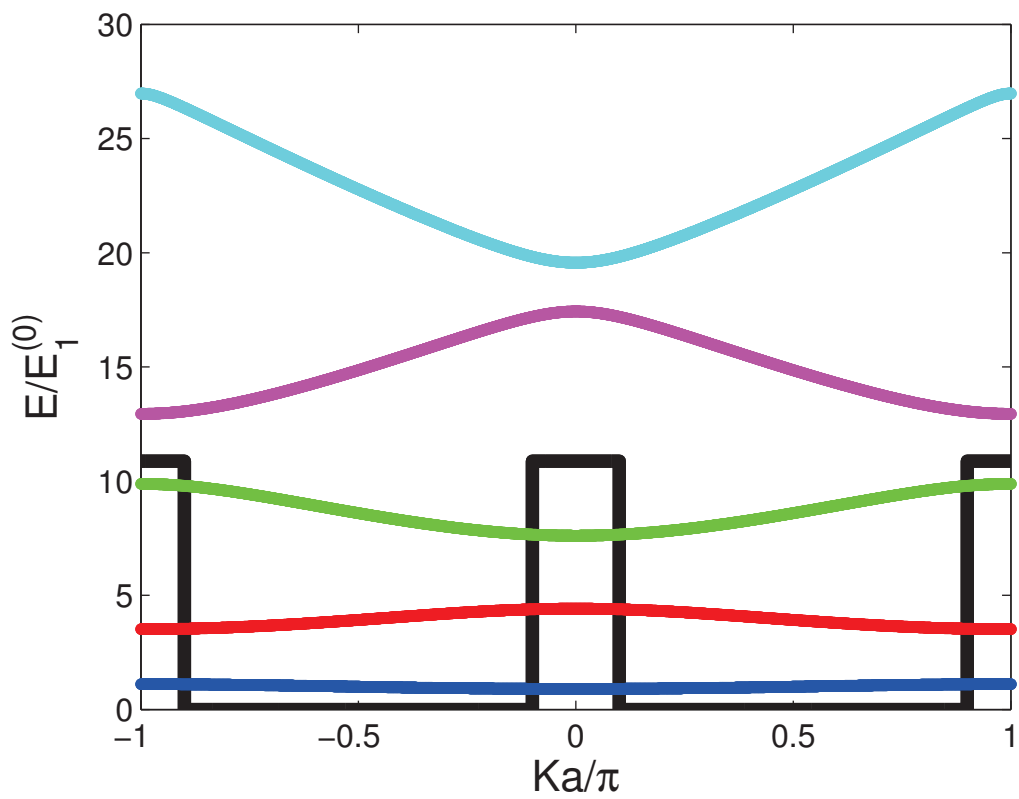
Figure 3.8: Energy band diagram for the Kronig-Penney potential with $\rho = 0.8$ and $v_0 = 10.8775$ (shown here schematically and also in Fig. 3.6b).
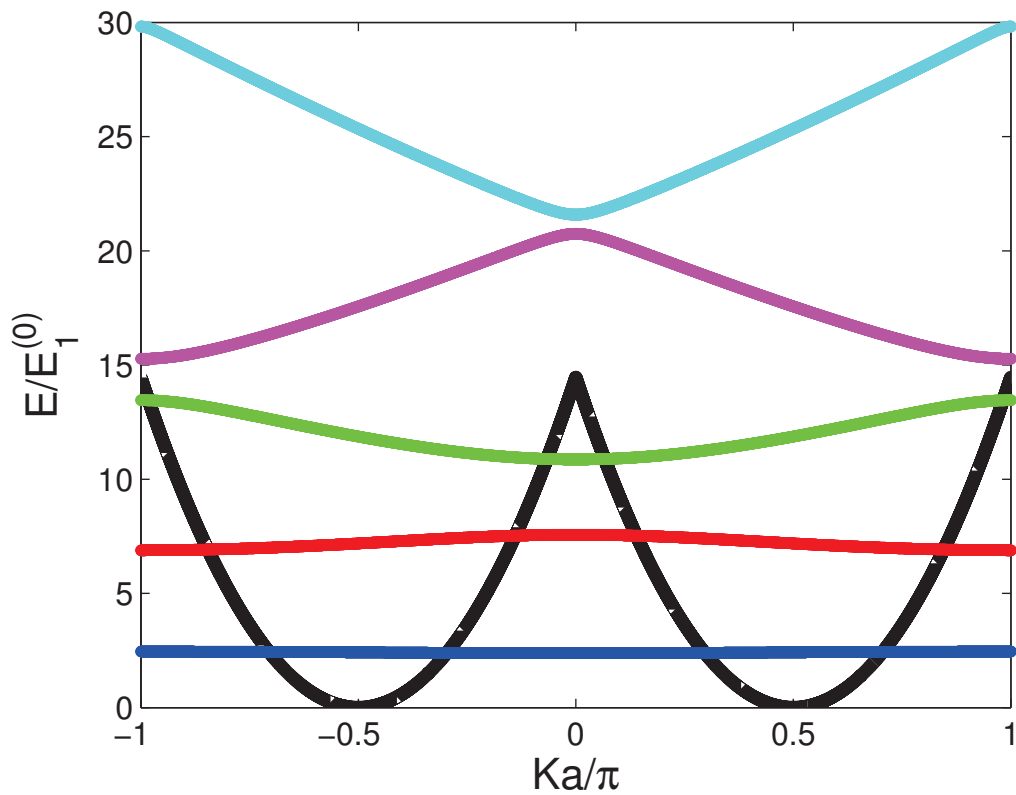
Figure 3.9: Energy band diagram for the simple harmonic oscillator potential with $\gamma = \hbar\omega/E_1^{(0)} = 4.84105$ (shown here schematically and also in Fig. 3.6c). Note the small energy gap separating the two highest energy bands (compared with that arising from the Kronig-Penney potential shown in the previous two figures). This gap is even smaller for the inverted harmonic oscillator potential (see Fig. 3.10) and the linear well potential (see Fig. 3.11).
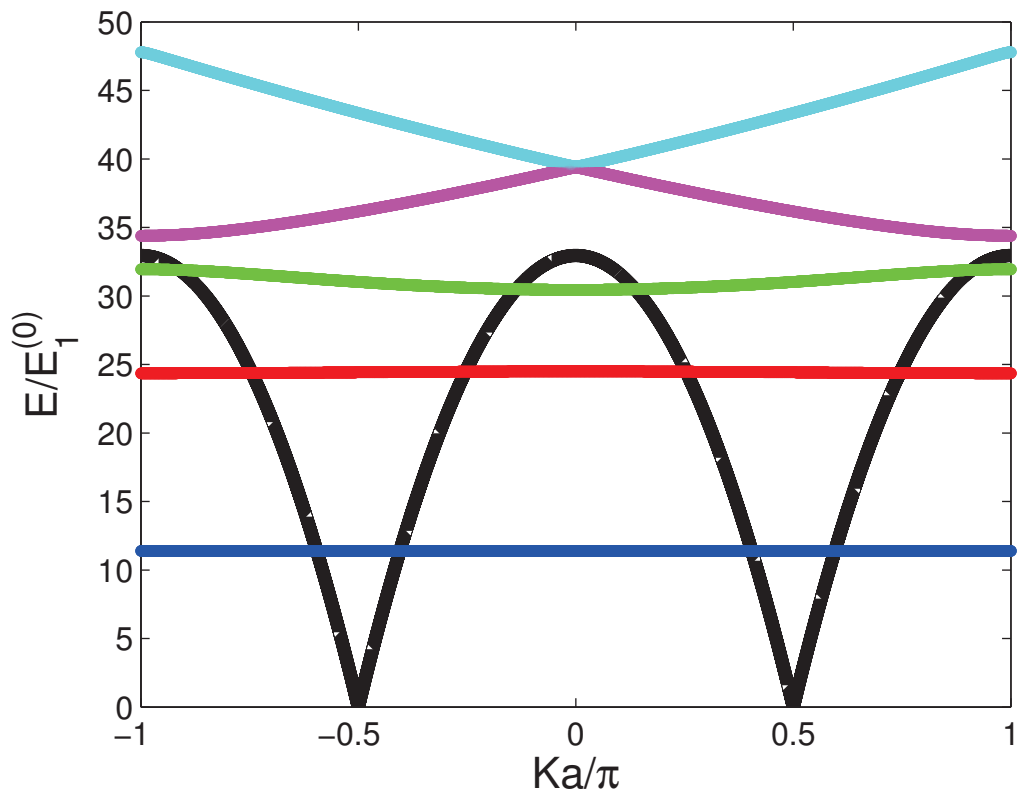
Figure 3.10: Energy band diagram for the inverted harmonic oscillator potential with $\gamma = \hbar\omega/E_1^{(0)} = 7.30845$ (shown here schematically and also in Fig. 3.6d). Note the very small gap between the two highest energy bands, and also the non-parabolic dispersion for these two bands.
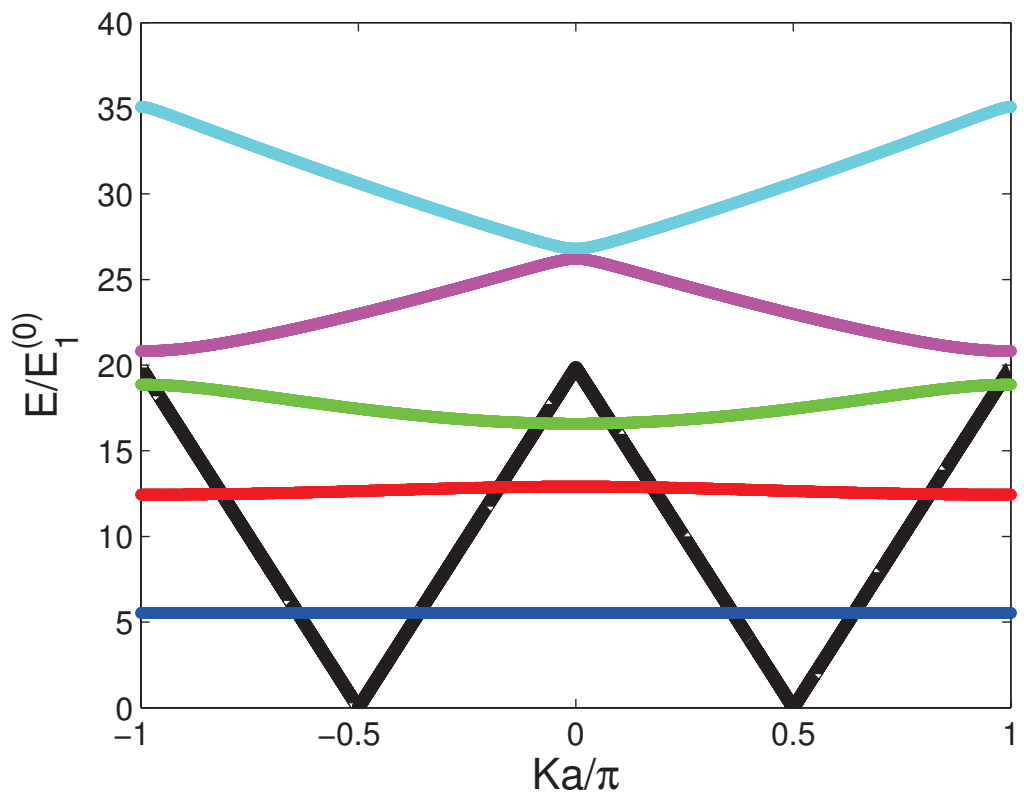
Figure 3.11: Energy band diagram for the linear well potential with $A = 19.8705$ (shown here schematically and also in Fig. 3.6e). The comments in the previous two figure captions apply here as well.
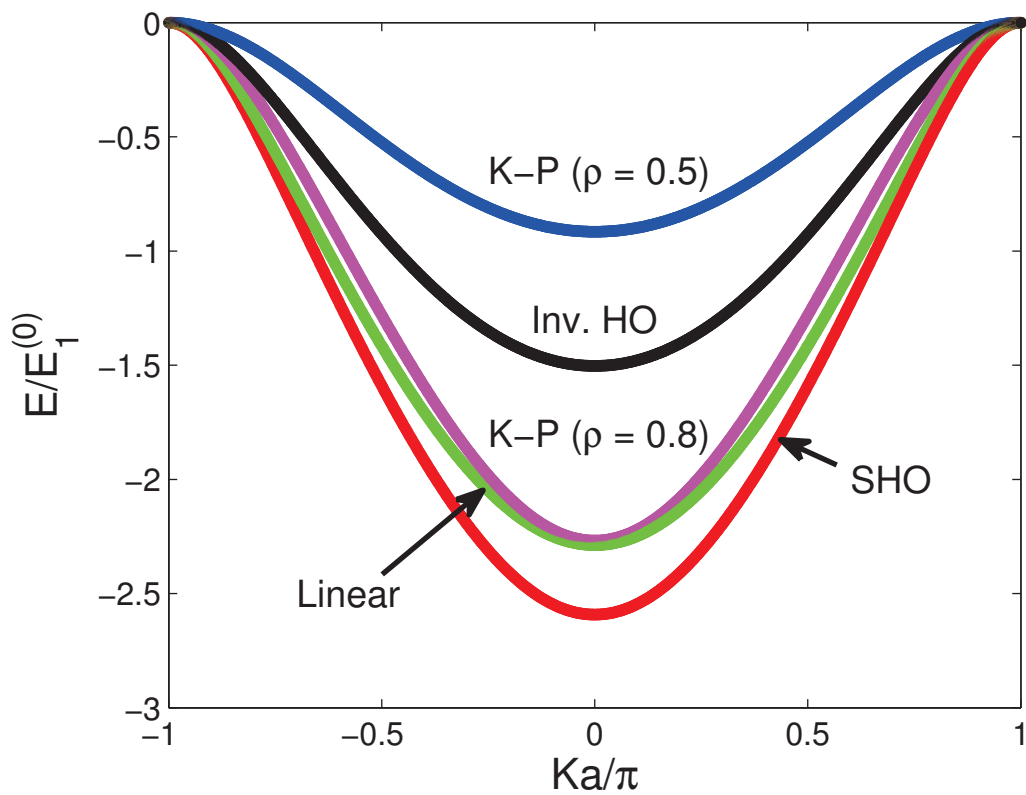
Figure 3.12: The third energy band for the five cases in Fig. 3.6, with the topmost energy set equal to zero. Note the variation in band width and, more importantly, the difference in curvatures, as tabulated in Table 3.3.

quite small (not discernible, for example, on the scale of Fig. 3.10). Moreover for these last three potentials, the minima and maxima of these higher energy bands can be distinctly non-parabolic, and in fact exhibit V-shaped (or inverted V-shaped) dispersions close to the minima (or maxima).

For each of these five potentials we then focused on the third band (the one closest to but lower than V_{max}), and normalized the bands by setting the highest band level to $E = 0$ in each case, as shown in Fig. 3.12. The band width varies considerably as shown; this can be adjusted by varying the barrier heights and widths, as is explicitly shown in the case of the Kronig-Penney model (first two parts of Fig. 3.6); in the case of the other potentials we could include an additional barrier or well "plateau."

3.5 Effective Masses

One property of importance is the ratio of the electron and hole effective masses. These are defined through the correspondence of the band dispersion with the free-electron-like parabolic behavior at the minima and maxima of the bands, respectively. It is well known in the semiconductor community that the hole effective mass at the top of the valence band can differ considerably from the electron effective mass at the bottom of the (next) conduction band. However, in the strongly-correlated-electron community many of the models utilized have electron-hole symmetry; this means that the electron and hole effective masses *in the same band* are identical. These effective masses are defined by

$$\frac{1}{m^*_{\substack{\mathrm{ele} \\ \mathrm{hol}}}} \equiv \frac{1}{\hbar^2} \frac{\mathrm{d}^2 E(K)}{\mathrm{d}K^2}\Bigg|_{\substack{K_{\mathrm{min}} \\ K_{\mathrm{max}}}}. \tag{3.38}$$

Derivations of this equation can be found in solid state physics textbooks, but a heuristic argument can be made by comparing to the free-electron case where the kinetic energy is given by $E = \hbar^2 K^2/(2m)$. In classical mechanics taking two derivatives of the kinetic energy with respect to the momentum gives the reciprocal of the mass, and so in our case we take derivatives with respect to the *crystal momentum* $\hbar K$ for the same effect.

We evaluate the second derivative in Eq. (3.38) using a five-point fit [23], and tabulate the ratio of the two effective masses for each potential shape in Table 3.3, where we also tabulate the dimensionless second derivatives $e_i'' \equiv (\pi^2/a^2)\,\mathrm{d}^2\,e_i(K)/\,\mathrm{d}K^2$, with $i = $ ele or hol. That is, these second derivatives are computed directly from the data points in Fig. 3.12 at the points $Ka/\pi = 0$ and 1. The ratio depends on the details of the potential used; the two Kronig-Penney models yield essentially the same

Table 3.3: The dimensionless second derivatives at the minimum (maximum) of the third energy bands from Fig. 3.12, which are inversely proportional to the electron and hole effective masses. The third column gives the ratio $e''_{\text{ele}}/e''_{\text{hol}} \equiv m^*_{\text{hol}}/m^*_{\text{ele}}$.

Potential	e''_{ele}	e''_{hol}	$e''_{\text{ele}}/e''_{\text{hol}}$
K-P ($\rho = 0.5$)	13.83	-25.35	-0.55
K-P ($\rho = 0.8$)	39.09	-70.61	-0.55
Simple HO	37.84	-121.80	-0.31
Inverted HO	19.83	-55.96	-0.35
Linear	31.63	-102.23	-0.31

ratio, and the magnitude of this ratio can decrease considerably with other potential shapes. First note that the ratio has a magnitude that is less than unity. This is because holes have effectively a weaker barrier through which to tunnel, compared with electrons. Consider the third band in any of Figs. 3.7, 3.8, 3.9, 3.10, or 3.11, and imagine two cases: the band is nearly empty of electrons (many holes) or the band is nearly full of electrons (few holes). For the nearly empty case, electrons will occupy the lowest-energy states near $K = 0$ and so, relative to their energy level, will see a higher potential step than in the case where the band is nearly filled with electrons near $K = \pm\pi/a$.

The decrease of this ratio below unity is most pronounced when either the linear or simple harmonic oscillator potential is used. The reason is that these have cusp-like barriers, so that the barrier width is also reduced for holes compared to electrons; therefore the holes should have more mobility (i.e., lower effective mass) compared with electrons, over and above the advantage already present due to the difference in effective barrier height. For Figs. 3.9, 3.10, and 3.11, looking at the third band once again, we see that the potentials "look" wider for those states around $K = 0$ than for those states near $K = \pm\pi/a$.

This asymmetry between electrons and holes may be important in a new class of superconducting models, where dynamic interactions are taken into account [25, 26].

3.6 An Alternative Approach

The method we have outlined in this chapter applies strictly to a lattice of infinite extent. We could also return to an infinite square well embedding potential and simply place in a finite number of rectangular barriers. An earlier approach similar to this methodology is Ref. [27]. Ref. [28] does exactly what we do in this section and

more, as they explicitly build on the Marsiglio research programme.

A representation of this model is shown in Fig. 3.13. While our unit cells have lattice spacing a, the overall well is of size L (where L is in units of a). If the centre of each well is situated as some position $\ell = \frac{1}{2}, \frac{3}{2}, \ldots L - \frac{1}{2}$ with barrier width b (again all in units of a) then

$$h_{nm}^v = v_0 \sum_\ell \int_{\ell - b/2}^{\ell + b/2} \mathrm{d}x \, \sin\left(\frac{n\pi x}{L}\right) \sin\left(\frac{m\pi x}{L}\right). \tag{3.39}$$

These integrals are easy to compute and have analytic solutions

$$h_{nm}^V = g_{nm}(\ell + b/2) - g_{nm}(\ell - b/2) \tag{3.40}$$

where

$$g_{nn}(s) = \frac{s}{L} - \frac{\sin(2\pi ns/L)}{2\pi n} \tag{3.41}$$

and

$$g_{nm}(s) = \frac{\sin\left[(m-n)\pi s/L\right]}{\pi(m-n)} - \frac{\sin\left[(m+n)\pi s/L\right]}{\pi(m+n)} \tag{3.42}$$

when $n \neq m$.
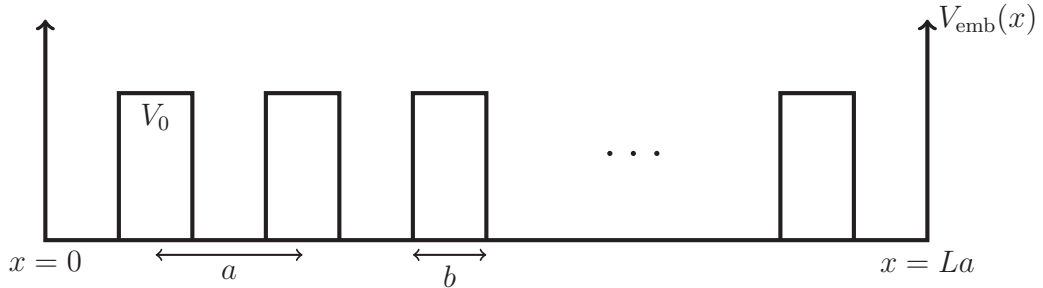
Figure 3.13: Representation of multiple unit cells in an infinite square well embedding potential.

With three free parameters (L, v_0, and b), there is clearly a large space of possible potentials we could sample. In Fig. 2 of [28] they chose $L = 10$, $b = 1/6$, and $v_0 = 100\pi^2$. In Fig. 3.14 we show some results for an arbitrary collection of those parameters.

We see clear splitting of the plane-wave parabola into energy bands as expected, with the number of solutions in each band corresponding to the number of barriers (or wells) L plus or minus one. This lack of constancy in the number of solutions per band likely arises from the peculiar "surface states" at the edges of the embedding well
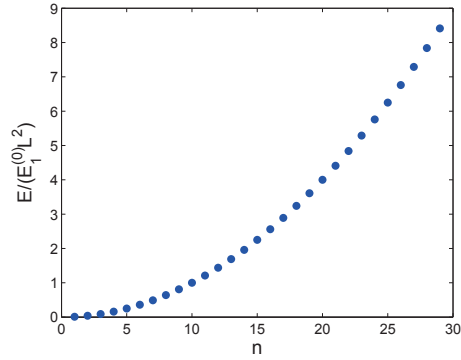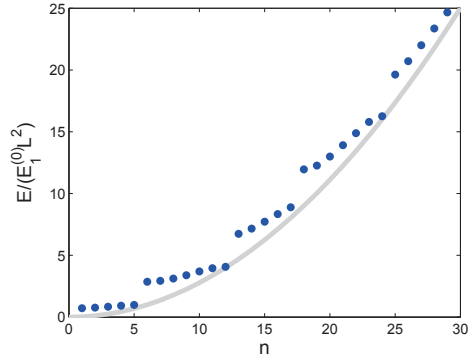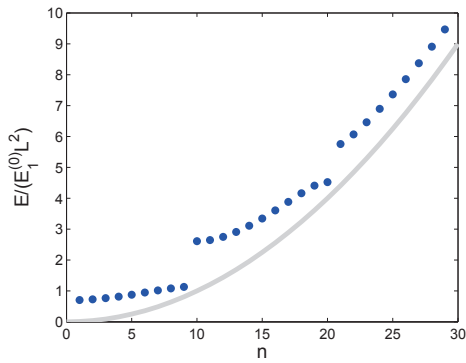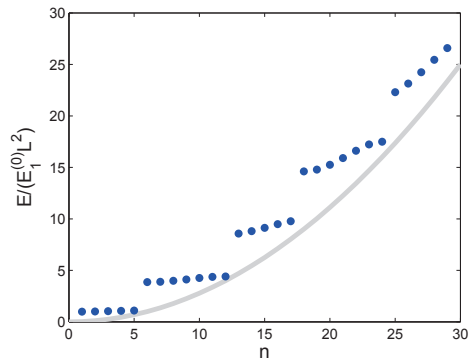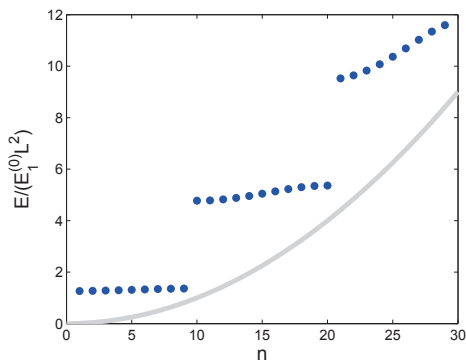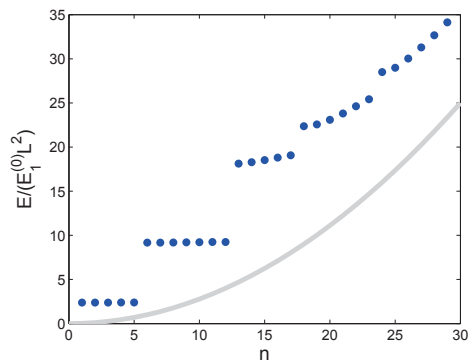
Figure 3.14: Energy spectrum for L rectangular wells of width b in an infinite square well embedding potential for various barrier heights v_0. The free electron parabola is displayed in light grey for reference.

44

which are forbidden from tunneling on one side. These inconsistencies are immaterial for large systems (in macroscopic solids of course $L \sim 10^{23}$).

Unlike the procedure for a general unit cell potential that we have developed in this chapter, the energy spectrum produced by the finite number of wells in an infinite square well embedding potential approach does not produce a reduced-zone scheme (which is what has been shown in all previous energy band diagrams). Rather, we see the "natural" splitting of the free electron parabola into bands. These bands could of course be shifted toward the origin to produce a reduced-zone scheme if desired.

We view this exercise as an interesting first step in the exploration of solid-state systems where even with just a few wells the energy band nature of periodic systems becomes manifest. After such an introduction, the full machinery we have developed in this chapter can then be developed which more accurately produces the band structure of "n large" systems.

3.7 Other Possibilities

We have by no means fully explored the space of one-dimensional periodic potentials here. Since the purpose of this work is to further develop physics pedagogy, our tool should leave ample room for exploration by students of many unforeseen models of interest.

For example, we here have limited ourselves to potentials that have analytical solutions for their matrix elements. That can of course be easily relaxed with the use of numerical integration procedures. One such potential of interest without known analytical solutions is the so-called "pseudo-Coulomb" potential

$$v(x) = \frac{V(x)}{E_1^{(0)}} = \frac{-A}{\sqrt{(x - a/2)^2 + b^2}}, \tag{3.43}$$

where A is a positive number representing the strength, or alternatively, the inverted pseudo-Coulomb potential with A negative, and where b is a small numerical factor introduced to prevent singularities (the true Coulomb potential is recovered as $b \to 0$).

We include a word of caution about potentials like Eq. (3.43) that are not a constant at the unit cell boundaries: if the potential still has some curvature at the unit cell boundary, repeating the unit cell will introduce an unphysical kink at those interfaces in the extended potential. An actual physical system would likely be continuously smooth.

Another potential of interest would be the linear diatomic lattice where each unit

cell contains two different atoms. A first approximation of this could be two square wells but with different depths.

Chapter 4

Two-Dimensional Potentials

In Chapter 3 we developed a matrix mechanics approach to periodic potentials in one dimension. In this chapter we extend that formalism to two-dimensional lattices with only a moderate increase in complexity. From this we can generate the electronic band structure of the "2D Kronig-Penney" model, as well as explore other potential shapes like the cylindrical "muffin-tin" potential as well as the Gaussian well. Extending further to multiple-atom supercells like the hexagonal lattice reveals the limit of this approach (the problem of zone folding), but our results still compare favourably to those found elsewhere in the literature.

4.1   Formalism

In two dimensions we introduce a rectangular unit cell with side lengths a_x and a_y obeying the general periodicity conditions

$$
\psi(x + a_x, y) = \psi(x, y)
$$
$$
\psi(x, y + a_y) = \psi(x, y). \tag{4.1}
$$

By separation of variables and the equivalent argument as in one dimension, we have basis states

$$
\psi^{(0)}_{n_x n_y}(x, y) = \frac{1}{\sqrt{a_x a_y}} \exp\left[i\frac{2\pi n_x}{a_x}x + i\frac{2\pi n_y}{a_y}y \right] \tag{4.2}
$$

where n_x and n_y are integers, with energy eigenvalues

$$
E^{(0)}_{n_x n_y} = 4 \left[n_x^2 + n_y^2 \left(\frac{a_x^2}{a_y^2} \right) \right] E_{\text{ISW}} = E^{(0)}_{n_x} + E^{(0)}_{n_y} \tag{4.3}
$$

47

by analogy with Eq. (2.16). The (a_x^2/a_y^2) term is to account for the fact that E_{ISW} is defined for length scale a_x. Whereas in previous chapters we have used $E_1^{(0)}$ to denote the infinite square well ground-state energy, at this point we simplify our notation a bit as the overall expressions become more complex. Of course, we could instead define E_{ISW} in terms of a_y in which case there would be an (a_y^2/a_x^2) in the $E_{n_x}^{(0)}$ component.

The Hamiltonian matrix elements will be of the form

$$
\begin{aligned}
H_{n_x n_y, m_x m_y} &= \langle \psi_{n_x n_y}^{(0)} | (H_0 + V) | \psi_{m_x m_y}^{(0)} \rangle \\
&= \delta_{n_x m_x} \delta_{n_y m_y} E_{n_x n_y}^{(0)} + H_{n_x n_y, m_x m_y}^{V}
\end{aligned}
\tag{4.4}
$$

where m_x and m_y are also integers.

In order to impose the Bloch condition, we modify Eq. (4.1) to

$$
\begin{aligned}
\psi(x + a_x, y) &= e^{iK_x a_x} \psi(x, y) \\
\psi(x, y + a_y) &= e^{iK_y a_y} \psi(x, y)
\end{aligned}
\tag{4.5}
$$

as was discussed in Section 3.1. Like the one-dimensional problem, the Bloch condition will only affect the kinetic energy terms. Following Eq. (3.4), we modify Eq. (4.3) to

$$
\begin{aligned}
E_{n_x}^{(0)} &= E_{\text{ISW}} \left(2n_x + \frac{K_x a_x}{\pi} \right)^2 \\
E_{n_y}^{(0)} &= E_{\text{ISW}} \left(2n_y + \frac{K_y a_y}{\pi} \right)^2 \left(\frac{a_x^2}{a_y^2} \right).
\end{aligned}
\tag{4.6}
$$

We have separated the two energy components here (and in later sections) for clarity, but of course there is only one summed energy $E_{n_x n_y}^{(0)}$, as in Eq. (4.3). The procedure then will be to compute the $K_x = K_y = 0$ Hamiltonian matrix case once, and then repeatedly diagonalize for different values of K_x and K_y which modify the Hamiltonian matrix per Eq. (4.6).

While our quantum numbers n_x, n_y, are integers, for computational reasons it is preferable to have a single natural number n to enumerate these states. Recall from Section 2.1.3 the transformation (Eq. (2.27))

$$
n = \frac{1 + (-1)^k (2k - 1)}{4}
\tag{4.7}
$$

to convert a natural number k to an ordered integer n. In two dimensions we generate two of these sequences, each extending from $-n_{\max}$ to $n_{\max}$, and interleave them as

$$(0,0),(0,1),(0,-1),\ldots(0,-n_{\max}),(1,0),(1,1),(1,-1)\ldots(1,-n_{\max}),(-1,0),(-1,1)\ldots$$

Finally, we sort these pairings (n_x, n_y) in an "increasing-energy encoding" by introducing some new $n_{\mathrm{sort}}^2 = n_x^2 + n_y^2$ variable and sorting it in ascending order which gives our final sequence

$$(n_x, n_y) = (0,0),(0,1),(0,-1),(1,0),(-1,0),(1,1),(1,-1),\ldots \rightarrow n = 1,2,3,4,5,6,7,\ldots \tag{4.8}$$

So for example the state $n = 7$ would represent the state with quantum numbers $(n_x, n_y) = (1, -1)$. We typically adopt some $n_{\max} = 7$, say. This means $-7 \leq n_x \leq 7$ and similarly for n_y. This results in $n = 1, 2, 3, \ldots (2n_{\max} + 1)^2$ i.e. $1 \leq n \leq 225$ for $n_{\max} = 7$, which means that we diagonalize a 255×255 matrix. We increase $n_{\max}$ until convergence to some desired level is attained.

While we can and will generate band structures for the whole "area" of K-space, it is useful (and for three-dimensional lattices, necessary), to trace a one-dimensional path through the two-dimensional K-space hitting "high-symmetry points" as we go. Following typical convention, we define some of these points (K_x, K_y) to be $\Gamma = (0,0)$, $X = (\pi/a_x, 0)$, $X' = (0, \pi/a_y)$, and $M = (\pi/a_x, \pi/a_y)$ (see Fig. 4.1). Most of the figures in this work will trace the triangular path $\Gamma \rightarrow X' \rightarrow M \rightarrow \Gamma$.
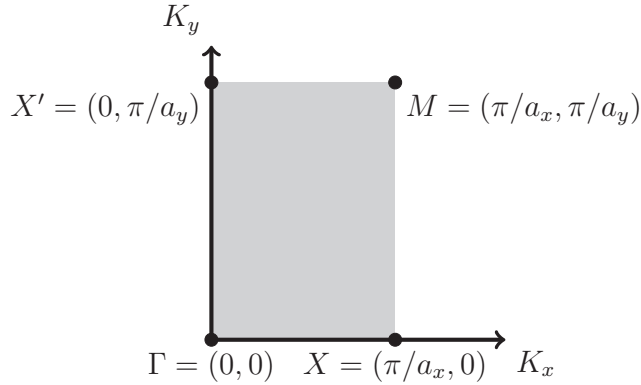
Figure 4.1: Representation in K-space of the location of the high-symmetry points in two dimensions. Similar symmetric points are found in the second, third, and fourth quadrants (not shown).

4.2   2D Kronig-Penney Model

We now introduce the so-called "2D Kronig Penney model," a straightforward extension of the one-dimensional case. In a square unit cell $a_x = a_y \equiv a$ (extending from 0 to a along both axes), we introduce a well with height V_0 (with dimensionless value $v_0 \equiv V_0/E_{\mathrm{ISW}}$), which will typically have a negative value, in the region

$$0 \leq q_1 \leq q_2 \leq a \tag{4.9}$$

for some fractional distances q_1 and q_2. In dimensionless form, these lengths will be normalized by the factor a and so we introduce $p_1 = q_1/a$ and $p_2 = q_2/a$ such that our now dimensionless distances obey

$$0 \leq p_1 \leq p_2 \leq 1. \tag{4.10}$$

The matrix elements for this potential are of the form

$$H^V_{n_x n_y, m_x m_y} = \frac{V_0}{a^2} \int_{q_1}^{q_2} \int_{q_1}^{q_2} \mathrm{d}x \, \mathrm{d}y \, e^{i2\pi(m_x - n_x)x/a} e^{i2\pi\left(m_y - n_y\right)y/a} \tag{4.11}$$

or in dimensionless form

$$h^V_{n_x n_y, m_x m_y} = v_0 \int_{p_1}^{p_2} \int_{p_1}^{p_2} \mathrm{d}x \, \mathrm{d}y \, e^{i2\pi(m_x - n_x)x} e^{i2\pi\left(m_y - n_y\right)y} \tag{4.12}$$

after making the transformation $x' = x/a$ and $y' = y/a$ and then dropping the dummy index primes for convenience. This double integration factors into a product of two one-dimensional integrals yielding

$$h^V_{n_x n_y, m_x m_y} = v_0 I(n_x, m_x) I(n_y, m_y) \tag{4.13}$$

where

$$I(n_j, m_j) = (p_2 - p_1)\, \delta_{n_j m_j} + i \frac{\left(e^{i2\pi(m_j - n_j)p_1} - e^{i2\pi(m_j - n_j)p_2}\right)}{2\pi(m_j - n_j)} \left(1 - \delta_{n_j m_j}\right). \tag{4.14}$$

where $j = x$ or y. Notice that for the main diagonal elements, the non-kinetic contribution will simply be the "volume" of the well, $v_0(p_2 - p_1)^2$, i.e. the "height" of the potential well multiplied by the fractional area of the unit cell that the well occupies. In general, we could position the well anywhere within the unit cell, so the

above integral could also be considered a function of p_1 and p_2. In this monograph we will typically center the well and most often use $p_1 = 1/4$ and $p_2 = 3/4$.

As a check, using the enumeration scheme explained by Eq. (4.7), we used the eigenstates produced by the diagonalization for $K_x = K_y = 0$ to produce the ground state wavefunction for various well depths, shown in Fig. 4.2. As expected, deeper wells more tightly constrain the wavefunction.

4.3   Nearly-free Electron Limit

For $v_0 = 0$, this approach will recapitulate the so-called empty lattice approximation with parabolic free electron bands, as shown in Figs. 4.3a and 4.3b. These are of course just the results you would get from plotting Eq. (4.6). Further, this method provides a convenient encoding scheme for the energy bands in terms of our chosen basis states. Consider the lowest energy branch going from Γ to X', ie. along the K_y-axis from 0 to π/a in Fig. 4.3b, where $n_x = 0$. Referring to Eq. (4.6), we can see that this lowest branch corresponds to $n_y = 0$, and only the $K_y a$ component contributes. The next higher energy branch corresponds to $n_y = -1$ as can be seen by direct substitution into the equation. Next is $n_y = +1$, and so on.

When we turn on v_0 for some small value, we enter the regime of the nearly-free electron model, whose salient feature is a lifting of degeneracies where band gaps emerge, and the sharp cusps for the $v_0 = 0$ case become smooth parabolas, as we can see in Fig. 4.3d (and to a lesser extent in Fig. 4.3c). Finally, we show results in Figs. 4.3e and 4.3f for an even deeper well, where an energy gap between the lowest band and the other bands exists for all wave vectors, reminiscent of the case in one dimension.

4.4   Tight Binding Limit

In the opposite limit for very deep wells we consider the tight binding model. Recall the stated result from Section 3.3,

$$\epsilon(\mathbf{K}) = \epsilon_0 - \sum_n t_n e^{i\mathbf{K}\boldsymbol{\delta}_n} \tag{4.15}$$

where now $\mathbf{K} = K_x \hat{\mathbf{x}} + K_y \hat{\mathbf{y}}$ in two dimensions. Even with vertical and horizontal symmetry ($a_x = a_y = a$), $\boldsymbol{\delta}_n$ takes on a more complicated general form as progressive nearest-neighbour lattice cells are not simply integer multiples of a. Nearest-

(a) $v_0 = 0$ (b) $v_0 = 0$

(c) $v_0 = -10$ (d) $v_0 = -10$

(e) $v_0 = -100$ (f) $v_0 = -100$
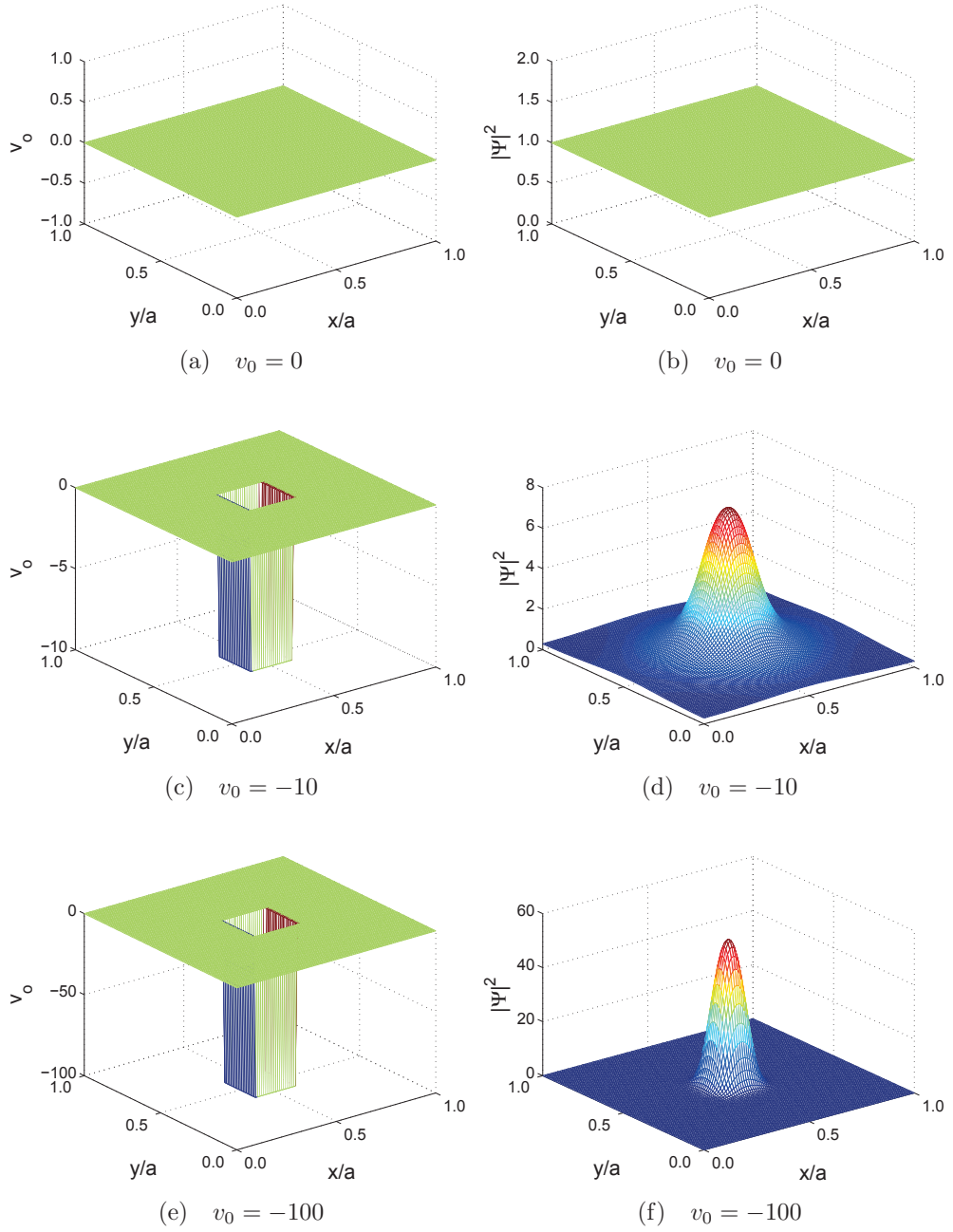
Figure 4.2: Representation of some 2D Kronig-Penney unit cell potentials (left column) and associated (non-Bloch modulated) wavefunctions (right column). Here $p_1 = 0.4$ and $p_2 = 0.6$.

(a) $v_0 = 0$

(b) $v_0 = 0$

(c) $v_0 = -1$

(d) $v_0 = -1$

(e) $v_0 = -3$

(f) $v_0 = -3$
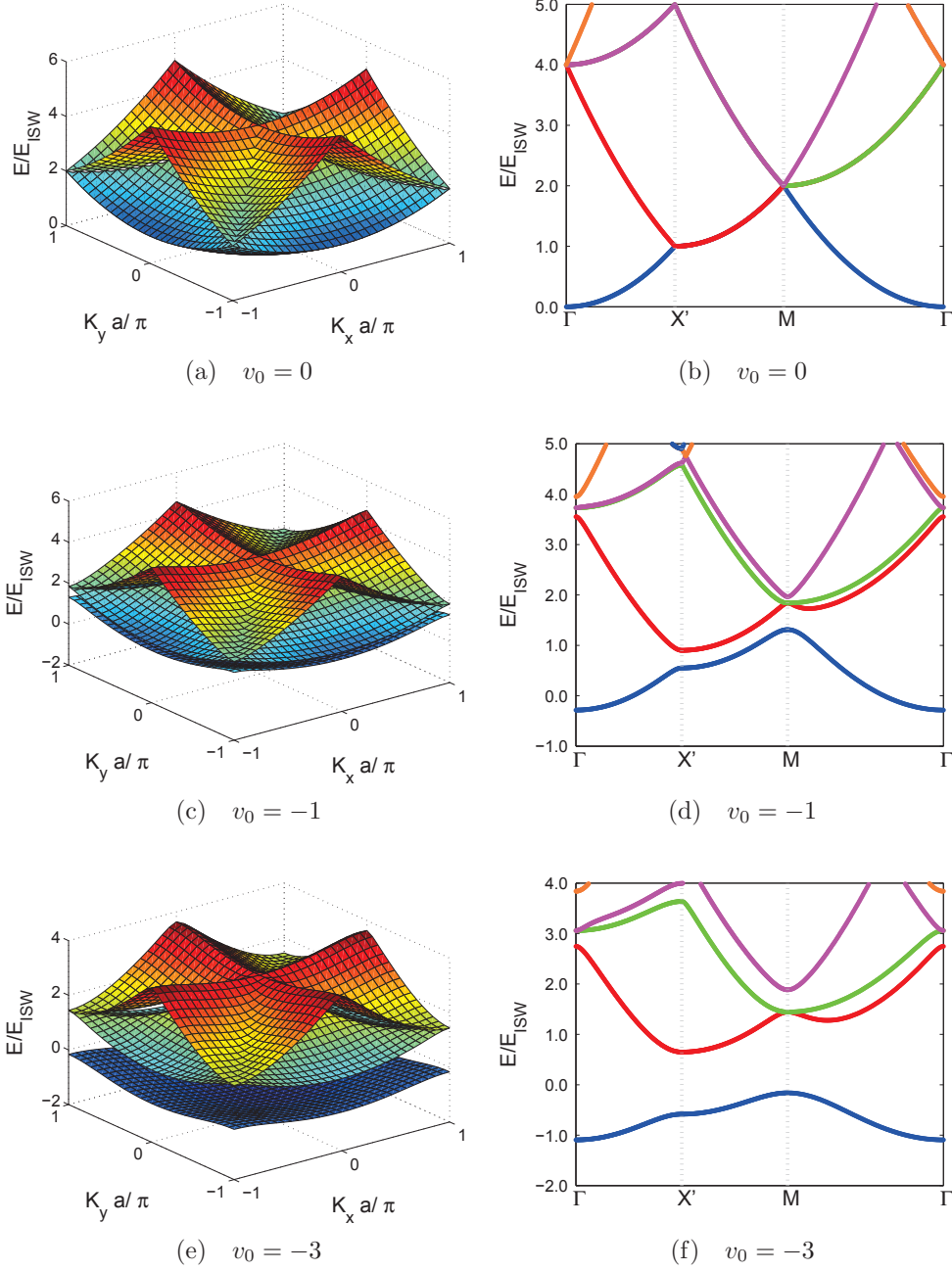
Figure 4.3: Generated band structures for various 2D Kronig-Penney well depths with $p_1 = 0.25$ and $p_2 = 0.75$. The full 3D representation is shown in the left column (for the first three energy bands) and the corresponding flattened plots for high-symmetry points is shown in the right column.
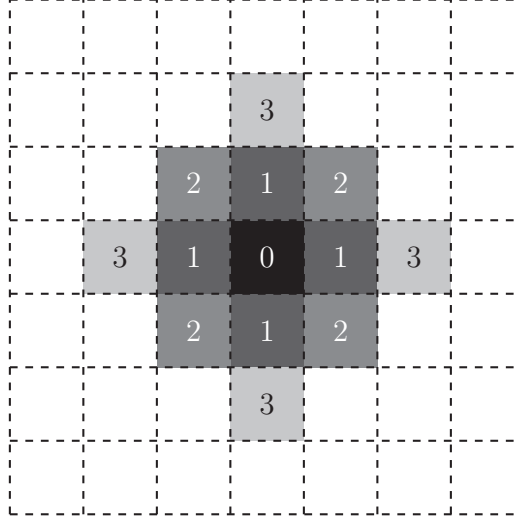
Figure 4.4: Representation of location of nearest-neighbour cells for the 2D square lattice as used in the tight binding model. 0 marks the ur-cell, 1 is nn, 2 is nnn, and 3 is nnnn.

neighbour hopping is simple enough to write out, with $\boldsymbol{\delta}_n = na\hat{\mathbf{x}}$ and $\boldsymbol{\delta}_n = na\hat{\mathbf{y}}$. Further nearest-neighbour effects can be inferred from Fig. 4.4. Thus restricting ourselves to just nearest-neighbour we have

$$\epsilon_{\mathrm{nn}}(K_x, K_y) = \epsilon_0 - 2t_1 \left[\cos(K_x a) + \cos(K_y a)\right] \tag{4.16}$$

where t_1 is the hopping integral. The next-nearest-neighbour (nnn) contribution is

$$\epsilon_{\mathrm{nnn}}(K_x, K_y) = \epsilon_{\mathrm{nn}}(K_x, K_y) - 2t_2 \left(\cos[(K_x + K_y)a] + \cos[(K_x - K_y)a]\right) \tag{4.17}$$

while next-next-nearest-neigbhour (nnnn) is

$$\epsilon_{\mathrm{nnnn}}(K_x, K_y) = \epsilon_{\mathrm{nnn}}(K_x, K_y) - 2t_3 \left[\cos(2K_x a) + \cos(2K_y a)\right]. \tag{4.18}$$

As before, what we are interested in is not the various t's themselves but the cosine behavior of the energy bands. The question is, as we make the well deeper and deeper, does the calculated energy band approach such a limit?

As our potential is symmetric, it does not matter which direction in K-space we choose, and so we arbitrarily select the K_y axis such that $K_x a = 0$. Then we numerically fit to the lowest-energy band a function $-2t\cos(\pi y) + E$ where "y" is our $K_y a/\pi$ result and E is a factor needed so the fitted curve is correctly situated vertically. The results are shown in Fig. 4.5. We see that as the well deepens,
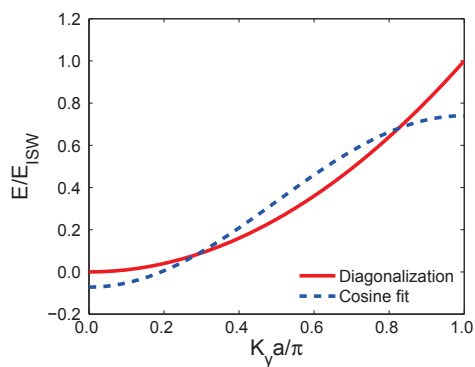
(a) $v_0 = 0, R^2 = 0.9234$
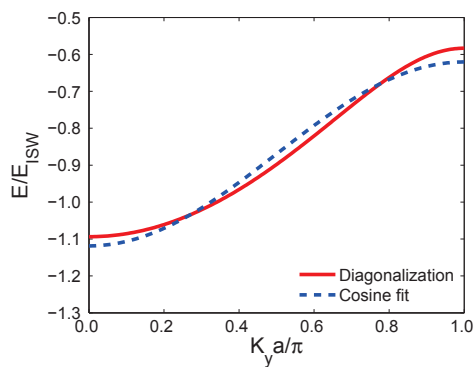
(b) $v_0 = -3, R^2 = 0.9854$
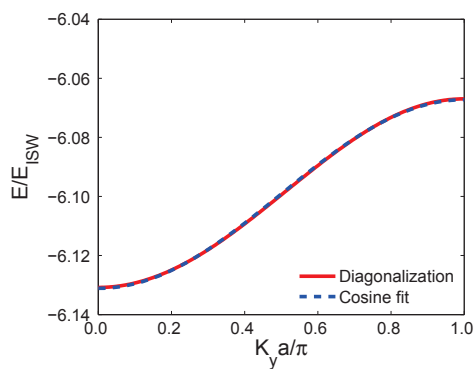
(c) $v_0 = -10, R^2 = 0.9999$

Figure 4.5: 2D Kronig-Penney results for the lowest-energy band with a fitted tight-binding cosine function, with $p_1 = 0.25$, $p_2 = 0.75$. As the well depth v_0 deepens, the results approach the tight-binding limit. Note especially in (b) the asymmetry between the top and bottom of the band. In (c) the curves are essentially on top of one another.

Table 4.1: Linear regression coefficients of determination (R^2) for tight binding fits to the 2D Kronig-Penney model, for nearest-neighbour (nn), next-nearest-neighbour (nnn), and next-next-nearest-neighbour.

v_0	nn	nnn	nnnn
0	0.9235	0.9235	0.9815
-1	0.9472	0.9472	0.9919
-3	0.9854	0.9854	0.9994
-10	0.9999	0.9999	1.0000

the diagonalization curve approaches the cosine fit, i.e. approaches the tight-binding limit as we'd expect. In the less extreme case (Fig. 4.5b) an asymmetry exists, and electron effective masses (related to the band curvature at $K_y = 0$) are larger than hole effective masses (related to the band curvature at $K_y = \pi/a$).

We can then do the same thing but fit to the more complicated expressions of Eqs. (4.17) and (4.18) as well. The results are shown in Table 4.1, where the same pattern we saw in Section 3.3 emerges: deeper wells and farther neighbour contributions improve the fit, exactly as we would expect.

This approach therefore offers a tool that students can use to check unfamiliar models like tight binding against this matrix mechanics approach. The further nearest-neighbour components can be successively introduced where they can see for themselves the improved convergence to the "true" solution. This tight feedback loop between computation and intuition-formation is the overall goal of this research programme.

Unfortunately, we cannot analytically determine and compare t_1 as we did in Section 3.3 since the analytical solution for the Kronig-Penney model itself does not exist in two dimensions.

4.5   Muffin-Tin Potential

We have used square potentials thus far; however, more realistic potentials arise through central forces, which necessitate a different $V(x, y)$. A more realistic potential is the so-called "muffin-tin potential," named for its resemblance to the depression in a muffin tin tray. Where the 2D Kronig-Penney potential was a repeating series of square wells in a square lattice, a muffin-tin potential is one with cylindrical wells. Such a potential imposes no conceptual difficulties, and the matrix elements are read-

ily expressed as (as in Section 4.2 we are using $a_x = a_y \equiv a$)

$$H^V_{n_x n_y, m_x m_y} = \frac{V_0}{a^2} \int_{\frac{a}{2}-r}^{\frac{a}{2}+r} \mathrm{d}x \int_{\frac{a}{2}-\sqrt{r^2-(x-\frac{a}{2})^2}}^{\frac{a}{2}+\sqrt{r^2-(x-\frac{a}{2})^2}} \mathrm{d}y \, e^{i2\pi(m_x-n_x)x/a} e^{i2\pi(m_y-n_y)y/a}. \quad (4.19)$$

The integral bounds come from the equation for a circle with radius r centered at $(x,y) = \left(\frac{a}{2}, \frac{a}{2}\right)$, namely

$$\left(x - \frac{a}{2}\right)^2 + \left(y - \frac{a}{2}\right)^2 = r^2. \quad (4.20)$$

As before the well depth is V_0 and will typically have a negative value. Positive V_0 would result in a series of cylindrical columns (which we might call the "Karnak potential" [43]). By making dimensionless substitutions $x/a \to x$, $y/a \to y$ as before, and defining $\bar{r} \equiv r/a$, we get

$$h^V_{n_x n_y, m_x m_y} = v_0 \int_{\frac{1}{2}-\bar{r}}^{\frac{1}{2}+\bar{r}} \mathrm{d}x \int_{\frac{1}{2}-\sqrt{\bar{r}^2-(x-\frac{1}{2})^2}}^{\frac{1}{2}+\sqrt{\bar{r}^2-(x-\frac{1}{2})^2}} \mathrm{d}y \, e^{i2\pi(m_x-n_x)x} e^{i2\pi(m_y-n_y)y}. \quad (4.21)$$

While the inner y integral is easily evaluated, we know of no analytic solution for the general matrix element. For the main diagonal matrix elements the exponentials reduce to unity and so the contribution is just the "volume" of a cylinder $\pi\bar{r}^2 v_0$ (recall the similar case for the rectangular 2D Kronig-Penney wells). For the off-diagonal elements we simply compute them numerically [35].

Some band structures for the muffin-tin potential are shown in Fig. 4.6. These results compare favorably to other methods found in the literature (see, for example, Fig. 5 in Ref. [29]). It takes appreciably more time to generate these figures than the 2D Kronig-Penney figures, due to having to compute the integrals numerically.

4.6 Gaussian Potential

The potentials mentioned so far have vertical walls with constant well depths. A more realistic potential would be smoothly varying (recall, however, the caveat from Section 3.7), and so we next turn to the two-dimensional Gaussian potential which has the form (again $a_x = a_y \equiv a$)

$$V(x,y) = V_0 \exp\left[-\left(\alpha_x \frac{(x-x_0)^2}{a^2} + \alpha_y \frac{(y-y_0)^2}{a^2}\right)\right] \quad (4.22)$$
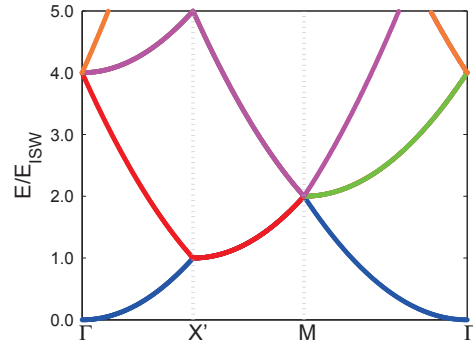
(a) $v_0 = 0$
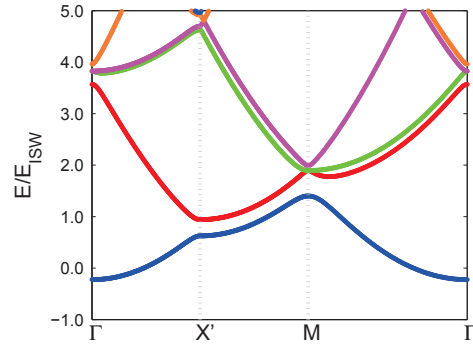
(b) $v_0 = -1$
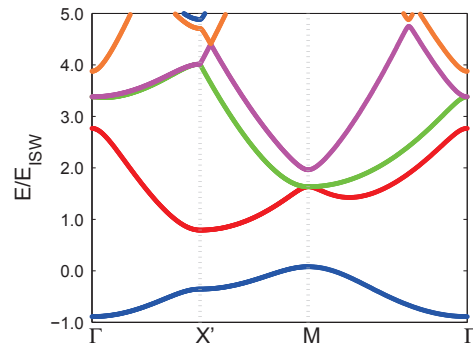
(c) $v_0 = -3$

Figure 4.6: Generated band structures for various muffin-tin well depths with $\bar{r} = 0.25$.

where V_0 represents the maximum depth of the well (and therefore typically takes on a negative value), (x_0, y_0) are the coordinates of the center of the well, and α_x and α_y are measures of the "range" of the well in either direction.

Like the 2D Kronig-Penney potential and unlike the muffin-tin potential, the Gaussian readily factorizes into two separate one-dimensional integrals. First we cast the problem into dimensionless form as we did in sections 4.2 and 4.5 and then we can write the matrix elements just like in Eq. 4.13 as

$$h^V_{n_x n_y, m_x m_y} = v_0 I(n_x, m_x, \alpha_x) I(n_y, m_y, \alpha_y) \tag{4.23}$$

where

$$I(n_j, m_j, \alpha_j) = \int_0^1 \mathrm{d}x \, e^{-\alpha_j (x - x_0)^2} e^{i 2\pi (m_j - n_j) x} \tag{4.24}$$

where $j = x, y$. This integral can be solved to give (we momentarily suppress the subscript j)

$$I(n, m, \alpha) = \tag{4.25}$$
$$\frac{1}{2} \sqrt{\frac{\pi}{\alpha}} e^{-\pi (m-n) \left[\pi (m-n) - 2i x_0 \alpha \right] / \alpha} \left(\mathrm{erf} \left[\frac{i\pi (m-n) + x_0 \alpha}{\sqrt{\alpha}} \right] - \mathrm{erf} \left[\frac{i\pi (m-n) + (x_0 - 1)\alpha}{\sqrt{\alpha}} \right] \right)$$

where

$$\mathrm{erf}(z) = \frac{2}{\sqrt{\pi}} \int_0^z \mathrm{d}t \, e^{-t^2} \tag{4.26}$$

is the error function. Though not strictly in a reduced analytical form, mathematics packages like Mathematica and MATLAB include built-in error function routines [31, 34]. For sufficiently large α, the error function terms in parentheses in Eq. 4.25 can be approximated as $\mathrm{erf}(\infty) - \mathrm{erf}(-\infty) = 2$. Otherwise, care should be taken to avoid overflowing the error function.

Plots of the band structure for various values of v_0 and α (where we have set $\alpha_x = \alpha_y = \alpha$ and placed the center of the well at the center of the unit cell) are shown in Fig. 4.7. There are no significant qualitative differences in the band structure obtained with this potential vs. the muffin tin potential, but comparison of Fig. 4.6 with Fig. 4.7 shows clear quantitative differences.

As was discussed in Section 3.7, we are in general hesitant to use such potentials that do not vanish at the boundaries of our unit cell. There will be sharp cusps in the potential at the unit cell boundaries, whereas we expect smooth wraparound in the cell since there is nothing intrinsically special about the boundaries when we obey

the general periodicity condition in Eq. 4.1. Thus, our mathematical model may not adhere to our desired smoothly-varying physical model.

The same applies, like in Section 3.7 to the 2D pseudo-Coulomb potential

$$V(x, y) = \frac{-V_0}{\sqrt{\left(x - a/2\right)^2 + \left(y - a/2\right)^2 + b^2}} \tag{4.27}$$

where b is some parameter introduced to prevent a singularity at the center. Such an integral must be computed numerically, but there are no further difficulties with the methodology for this model, however.

4.7 Two-Atom Unit Cell

We have thus far limited ourselves to one atom per unit cell, but it is of interest for more complicated structures that we relax this restriction. To begin, we consider again the 2D Kronig-Penney model but viewed through a larger "window," with a rectangle consisting of two of the previously discussed unit cells. That is, we'll consider a rectangle with side lengths a_x and a_y where $a_x = 2a_y$ for the x- and y-directions respectively, with two square wells centered at $(x_1, y_1) = (a_x/2, a_y/2)$ and $(x_2, y_2) = (3a_x/2, a_y/2)$. Physically, this is identical to the model with a square unit cell considered in section III.

We can then compute for the Hamiltonian elements

$$H^V_{n_x n_y, m_x m_y} = \frac{V_0}{a_x a_y} \left(\int_{a_x/4}^{3a_x/4} + \int_{5a_x/4}^{7a_x/4} \right) \mathrm{d}x \, e^{i2\pi(m_x - n_x)x/a_x} \int_{a_y/4}^{3a_y/4} \mathrm{d}y \, e^{i2\pi\left(m_y - n_y\right)y/a_y} \tag{4.28}$$

or in dimensionless form

$$h^V_{n_x n_y, m_x m_y} = v_0 \left(\int_{1/4}^{3/4} + \int_{5/4}^{7/4} \right) \mathrm{d}x \, e^{i2\pi(m_x - n_x)x} \int_{1/4}^{3/4} \mathrm{d}y \, e^{i2\pi\left(m_y - n_y\right)y}. \tag{4.29}$$

We have written the x integrals in a slightly peculiar way; all we mean to say is that we compute two integrals with the separate bounds of the two wells but with the same integrand, and the y integral distributes over these two multiplicatively.

60
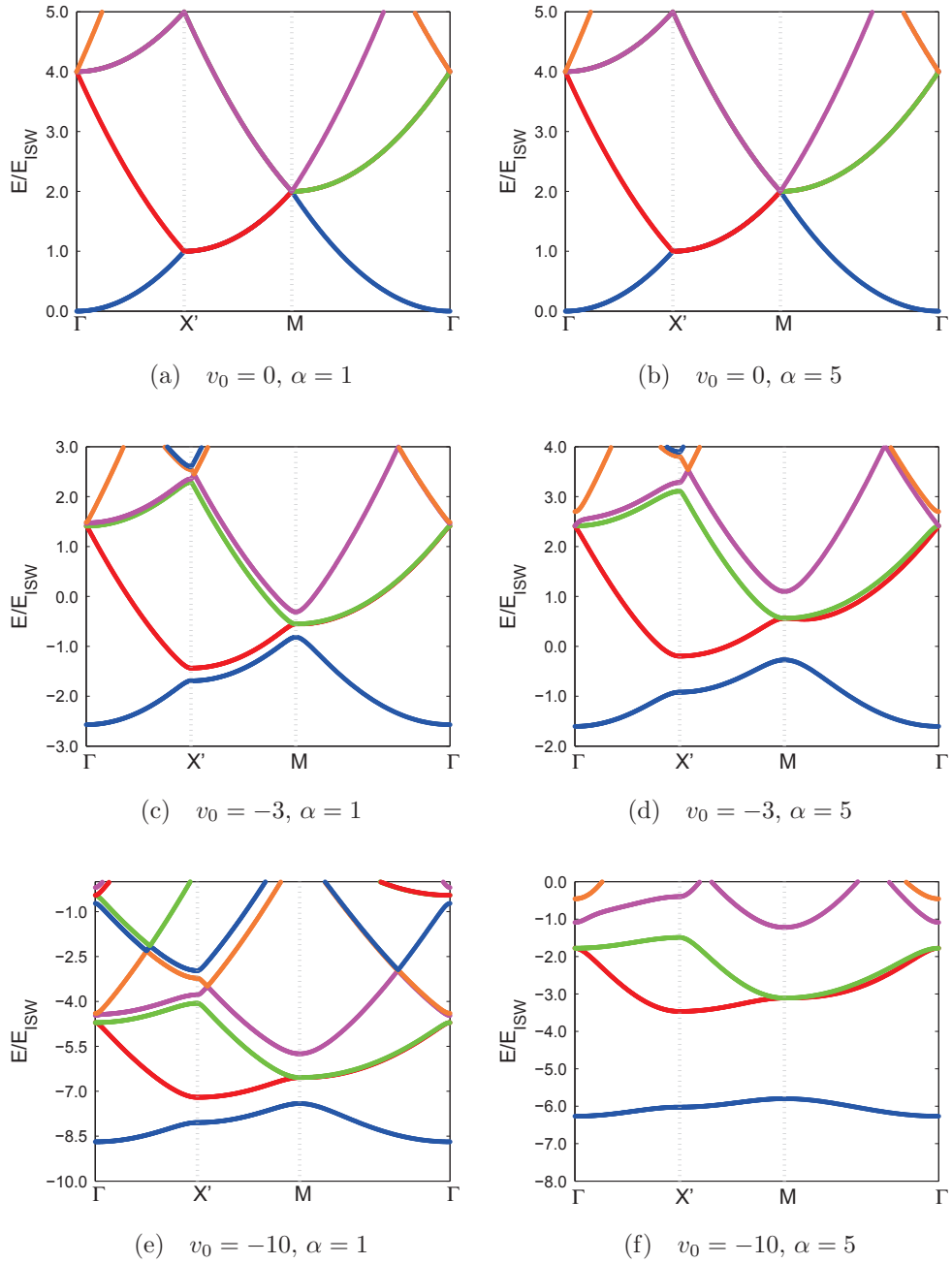
Figure 4.7: Generated band structures for various Gaussian wells. Here $\alpha_x = \alpha_y = \alpha$ and $(\frac{x_0}{a}, \frac{y_0}{a}) = (\frac{1}{2}, \frac{1}{2})$. There are no significant differences with the bands generated with muffin-tin potentials in Fig. 4.6.

61

We now rewrite Eq. (4.6) with the substitution $a_x = 2a_y$ giving

$$E_{n_x}^{(0)} = E_{\text{ISW}} \left(2n_x + \frac{K_x a_x}{\pi} \right)^2$$

$$E_{n_y}^{(0)} = E_{\text{ISW}} \left(4n_y + \frac{K_y a_x}{\pi} \right)^2. \tag{4.30}$$

We have written both energy components in terms of just one length parameter (in this case, arbitrarily a_x) for computational convenience. We recall that while we have written Eq. (4.30) as two separate terms for clarity, there is only one energy level $E_{n_x n_y}^{(0)} = E_{n_x}^{(0)} + E_{n_y}^{(0)}$ for any given $(K_x a_x, K_y a_x)$.

In Fig. 4.8 we show the generated band structure for $v_0 = 0$. Now, $X' = (0, \pi/a_y) = (0, 2\pi/a_x)$. As usual we have used colors to distinguish when eigenenergies are being plotted, but since the electronic branches cross each other in places we see that the eigenenergy ordering does not correspond necessarily to physical meaningful branch ordering.
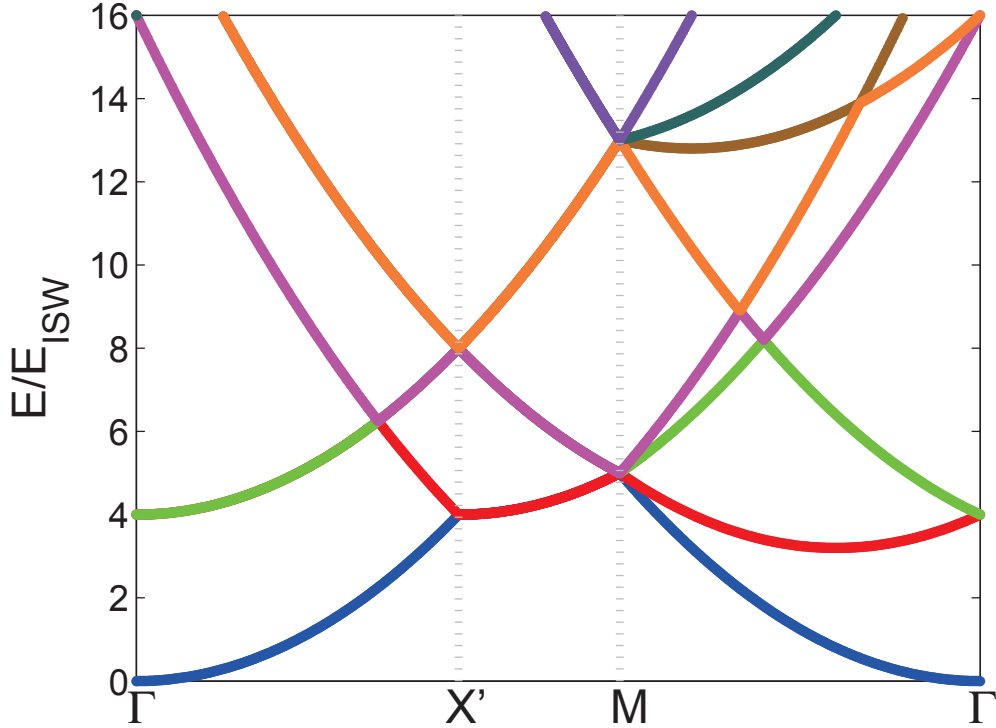
Figure 4.8: Generated band structure for the two-site rectangular cell for $v_0 = 0$. Note the clear difference from Fig. 4.3b due to zone folding.

Clearly, Fig. 4.8 is different from Fig. 4.3b. This is a general problem in electronic band structure calculations where the use of a non-primitive unit cell (i.e. not the Wigner-Seitz cell) produces a band diagram that contains extra information compared to the first Brillouin zone corresponding to the primitive cell [38]. Primitive cells, however, are often complicated geometrically with difficult-to-satisfy boundary conditions, making calculations more intractable. Techniques exist to "zone unfold" the band diagrams from non-primitive cells into their Brillouin zone analogues [40]. We will further discuss zone unfolding in Section 6.1.

4.8 Hexagonal Lattice

Hexagonal lattices are typically tiled with rhomboid unit cells using a two atom-per-site basis. Our matrix mechanics method is more easily implemented with a rectangular cell, however, in order to easily use the plane-wave basis state expansion. A rectangular tiling can be accomplished with the unit cell shown in Fig. 4.9a. This is likely not immediately obvious, but laying out a grid of such cells will show the hexagonal pattern emerging. If the "bond length" of the hexagonal lattice is called δ, the dimensions of the rectangle are $3\delta \times \sqrt{3}\delta$ with the "atomic" sites located at $(\frac{1}{2}\delta, \frac{\sqrt{3}}{4}\delta), (\delta, \frac{3\sqrt{3}}{4}\delta), (2\delta, \frac{3\sqrt{3}}{4}\delta), (\frac{5}{2}\delta, \frac{\sqrt{3}}{4}\delta)$. Showing this is a fairly simple exercise in geometry. Our basis states will then be as in Eq. 4.2 with $a_x = 3\delta$ and $a_y = \sqrt{3}\delta$. Here we have chosen square wells with a width of $\frac{1}{2}\delta$. One can then use matrix elements as per Eqs. (4.13) and (4.14) with appropriately chosen p values. Further, the relative energy scaling in Eq. (4.6) must be taken into account, where we have $(a_x^2/a_y^2) = (a_x^2/(\frac{\sqrt{3}}{3}a_x)^2) = 3$, giving (when we rewrite in terms of a_x as we did in Eq. (4.30))

$$
\begin{aligned}
E_{n_x}^{(0)} &= E_{\text{ISW}} \left(2n_x + \frac{K_x a_x}{\pi} \right)^2 \\
E_{n_y}^{(0)} &= E_{\text{ISW}} \left(3 \cdot 4n_y^2 + \left(\frac{3}{\sqrt{3}} \right) 4\frac{n_y K_y a_x}{\pi} + \left(\frac{K_y a_x}{\pi} \right)^2 \right) \\
&= E_{\text{ISW}} \left(2\sqrt{3}n_y + \frac{K_y a_x}{\pi} \right)^2 .
\end{aligned}
\tag{4.31}
$$

From a diagonalization of such a matrix, we can reconstruct the ground state wavefunction as a check, which we have done in Fig. 4.9b, showing appropriate localization in the wells. We can then use all the usual machinery to generate the energy band structure of this potential, which we have done for $v_0 = -20$ in Fig. 4.10a.

63
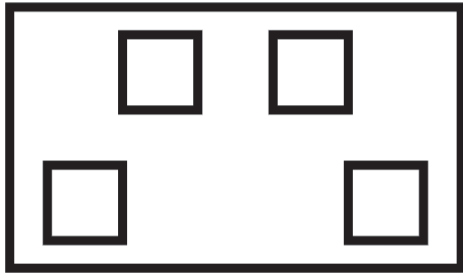
(a) Schematic representation with correct relative sizes of the unit cell structures (square wells).
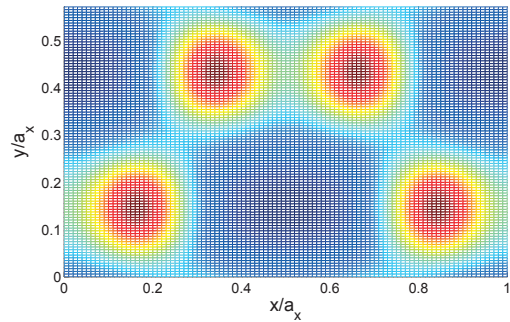
(b) Countour map of the ground state wavefunction (square wells). Note the lack of hexagonal symmetry in the wave functions due to the square potentials.
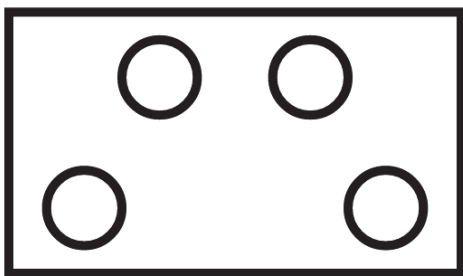
(c) Schematic representation with correct relative sizes of the unit cell structures (muffin-tin wells).
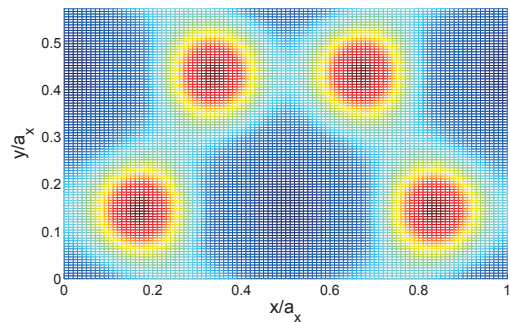
(d) Countour map of the ground state wavefunction (muffin-tin wells). Hexagonal symmetry is clearly present. Compare with (b).

Figure 4.9: The rectangular unit cell for the hexagonal lattice, both a schematic representation of the placement of the square wells and the contour map of the ground state wavefunction. Top row is for square wells, bottom row is for muffin-tin wells. $v_0 = -5$ in both cases.

We see a pattern highly suggestive of Dirac cones [39] in the band structure. This is remarkable because our model is fairly simple, using only square wells. Such wells break the expected hexagonal symmetry, so a more realistic potential would have radially-symmetric wells, like the circular muffin-tin wells we explored in Section 4.5. This is easily done using numerical integration, though the time for computation is much slower than for the analytic square well case.

To demonstrate the procedure, we now derive the integral for the well located at $(\frac{1}{2}\delta, \frac{\sqrt{3}}{4}\delta) = (\frac{a_x}{6}, \frac{a_y}{4}) = (\frac{a_x}{6}, \frac{\sqrt{3}a_x}{12})$. We will use $\frac{r}{a_x} = \frac{1}{12}$ to keep rough parity with the square wells. Here r is the radius of the muffin-tin well. Fig. 4.9c shows what such a unit cell looks like, and Fig. 4.9d serves as a check where we have reconstructed the ground state wavefunction. Note that with the radially-symmetric wells we do get the expected hexagonal symmetry, as there is now no preferred direction for the wavefunction adjoining the wells.

The equation for such a circle is

$$
\left(x - \frac{a_x}{6}\right)^2 + \left(y - \frac{a_x\sqrt{3}}{12}\right)^2 = r^2.
\tag{4.32}
$$

Like Eq. (4.19) we can write

$$
H_{n_x n_y, m_x m_y}^V = \frac{V_0}{a_x a_y} \int_{\frac{a_x}{6}-r}^{\frac{a_x}{6}+r} \mathrm{d}x \int_{\frac{a_x\sqrt{3}}{12}-\sqrt{r^2-(x-\frac{a_x}{6})^2}}^{\frac{a_x\sqrt{3}}{12}+\sqrt{r^2-(x-\frac{a_x}{6})^2}} \mathrm{d}y\, e^{i2\pi(m_x-n_x)x/a_x} e^{i2\pi\left(m_y-n_y\right)y/a_y}
\tag{4.33}
$$

or writing $a_y = a_x\sqrt{3}/3$ and making making the equation dimensionless as we've done previously ($x/a_x \to x$, $y/a_x \to y$, and $\bar{r} \equiv r/a_x$) we get

$$
h_{n_x n_y, m_x m_y}^V = v_0\sqrt{3} \int_{\frac{1}{6}-\bar{r}}^{\frac{1}{6}+\bar{r}} \mathrm{d}x \int_{\frac{\sqrt{3}}{12}-\sqrt{\bar{r}^2-(x-\frac{1}{6})^2}}^{\frac{\sqrt{3}}{12}+\sqrt{\bar{r}^2-(x-\frac{1}{6})^2}} \mathrm{d}y\, e^{i2\pi(m_x-n_x)x} e^{i2\pi\left(m_y-n_y\right)y/(\sqrt{3}/3)}
\tag{4.34}
$$

We generate band structures as shown in Fig. 4.10b. Again we see structures highly suggestive of Dirac cones, and the results using muffin tins are qualitatively similar to the results using square wells.

We can then easily expand around the Dirac points to get a more detailed view, as shown in Figs. 4.10c and 4.10d. To verify that these cones have linear dispersion, we expand yet further along a cross-section through $K_x = 0$, shown in Figs. 4.10e and 4.10f. We find these structures clearly exhibit a conical shape with linear dispersion. Remarkably, these structures are present even in the relatively crude model using

square wells.

However, as was evident in Section 4.7, our results are not directly comparable to the known locations of Dirac cones for the hexagonal lattice in the Brillouin zone. *Ab initio* band structures for graphene are presented in Ref. [41], for example, but direct comparison is impossible, first because of the unfolding difficulty, but also because we utilize much simpler potentials. Nonetheless, we can compare our results to other work that uses a similar tiling schema for the case of a hexagonal graphene lattice. Using the rectangular high-symmetry points $\Gamma = (0,0)$, $X = (\pi/a_x, 0)$, $X' = (0, \pi/a_y)$, and $M = (\pi/a_x, \pi/a_y)$ we can generate Fig. 4.11 which has excellent qualitative correspondence with Fig. 2d of Ref. [42]. In that work such a band diagram was successfully unfolded using an unfolding program of the authors' construction. We have also obtained results for square well potentials; these are not shown as they are very similar to those shown in Fig. 4.11.
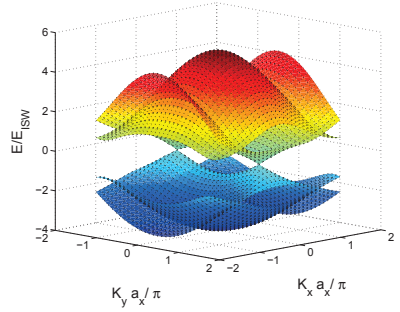
(a)　First four bands, square wells.
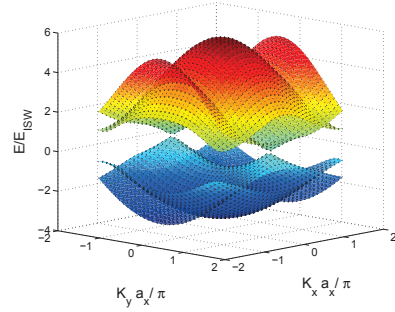
(b)　First four bands, muffin-tin wells.
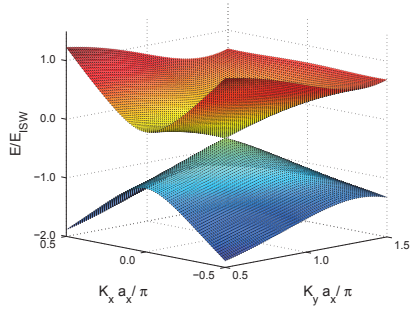
(c)　Expansion of the second and third bands around possible Dirac cone, square wells.
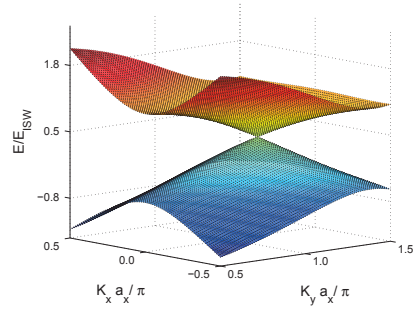
(d)　Expansion of the second and third bands around possible Dirac cone, muffin-tin wells.
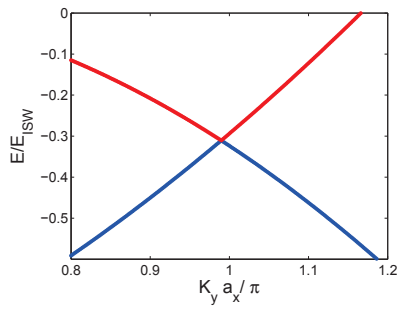
(e)　Cross-section for $K_x = 0$ of the second and third bands around Dirac cone point, square wells.
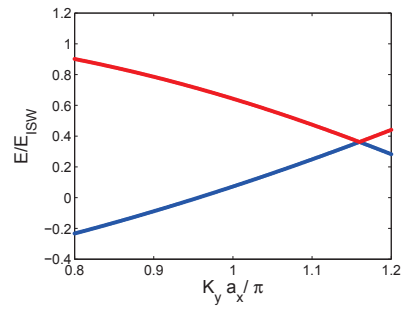
(f)　Cross-section for $K_x = 0$ of the second and third bands around Dirac cone point, muffin-tin wells.

Figure 4.10: Generated band structures for the hexagonal lattice, with square wells in the left column and cylindrical muffin-tin wells in the right column, both with $v_0 = -20$.
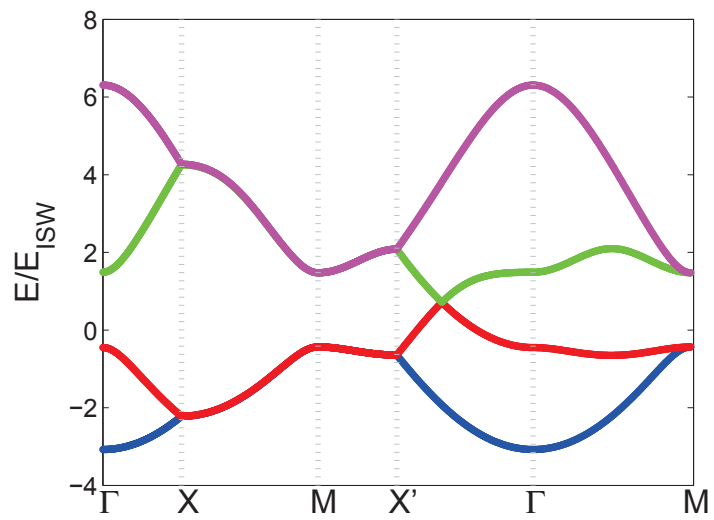
Figure 4.11: Generated band structure for the hexagonal lattice using muffin-tin wells with $v_0 = -19$. This output is qualitatively very similar to Fig. 2d of Ref. [42].

Chapter 5

Three-Dimensional Potentials

The extension of our matrix mechanics approach from one dimension to two dimensions was easily accomplished by our choice of plane-wave basis states in a rectangular unit cell. Likewise, we can extend to three dimensions readily by choosing a rectangular prism unit cell. Generating band structure diagrams for the "3D Kronig-Penney model" is easily accomplished by now, though the problem of unfolding that was present in our analysis of 2D problems is yet even greater in three dimensions. While we sketch out how to use this approach for other lattice types like face-centered cubic (fcc) and body-centered cubic (bcc), until the problem of unfolding is addressed the actual computation for those potentials is of limited interest.

5.1 Formalism

We construct a rectangular prism unit cell of side lengths (a_x, a_y, a_z) that obeys the general periodicity in each direction (a 3-torus),

$$
\begin{aligned}
\psi(x + a_x, y, z) &= \psi(x, y, z) \\
\psi(x, y + a_y, z) &= \psi(x, y, z) \\
\psi(x, y, z + a_z) &= \psi(x, y, z).
\end{aligned}
\tag{5.1}
$$

These will have plane-wave basis states

$$
\psi^{(0)}_{n_x n_y n_z}(x, y, z) = \frac{1}{\sqrt{a_x a_y a_z}} \exp\left[i \frac{2\pi n_x}{a_x} x + i \frac{2\pi n_y}{a_y} y + i \frac{2\pi n_z}{a_z} z \right]
\tag{5.2}
$$

(where n_x, n_y, and n_z are integers) with energy eigenstates

$$E^{(0)}_{n_x n_y n_z} = 4 \left[n_x^2 + n_y^2 \left(\frac{a_x^2}{a_y^2} \right) + n_z^2 \left(\frac{a_x^2}{a_z^2} \right) \right] E_\text{ISW} = E^{(0)}_{n_x} + E^{(0)}_{n_y} \left(\frac{a_x^2}{a_y^2} \right) + E^{(0)}_{n_z} \left(\frac{a_x^2}{a_z^2} \right)$$

(5.3)

where

$$E_\text{ISW} = \frac{\hbar^2 \pi^2}{2 m_0 a_x^2}$$

(5.4)

is the infinite square well ground state energy (periodic-boundary condition wells have four times this energy). The (a_x^2/a_y^2) and (a_x^2/a_z^2) terms in Eq. (5.3) are to account for the fact that we've defined E_ISW in terms of the length a_x. It should be fairly clear that this arbitrary decision is easy to change so long as the ratios are moved to the correct terms and suitably inverted.

We then introduce some potential $V(x, y, z)$ into our unit cell and solve the matrix mechanics problem

$$\begin{aligned} H_{n_x n_y n_z, m_x m_y m_z} &= \langle \psi^{(0)}_{n_x n_y n_z} | (H_0 + V) | \psi^{(0)}_{m_x m_y m_z} \rangle \\ &= \delta_{n_x m_x} \delta_{n_y m_y} \delta_{n_z m_z} E^{(0)}_{n_x n_y n_z} + H^V_{n_x n_y n_z, m_x m_y m_z} \end{aligned}$$

(5.5)

(where m_x, m_y, and m_z are also integers) and

$$H_0 = -\frac{\hbar^2}{2 m_0} \nabla^2$$

(5.6)

gives the kinetic energy terms in the matrix. For $V(x, y, z) = 0$ then, this will simply return the free electron quadratic bands.

As before we then introduce the Bloch condition

$$\begin{aligned} \psi(x + a_x, y, z) &= e^{iK_x a_x} \psi(x, y, z) \\ \psi(x, y + a_y, z) &= e^{iK_y a_y} \psi(x, y, z) \\ \psi(x, y, z + a_z) &= e^{iK_z a_z} \psi(x, y, z) \end{aligned}$$

(5.7)

which modifies the energy terms as

$$E_{n_x}^{(0)} = E_{\text{ISW}} \left(2n_x + \frac{K_x a_x}{\pi} \right)^2$$

$$E_{n_y}^{(0)} = E_{\text{ISW}} \left(2n_y + \frac{K_y a_y}{\pi} \right)^2 \left(\frac{a_x^2}{a_y^2} \right)$$

$$E_{n_z}^{(0)} = E_{\text{ISW}} \left(2n_z + \frac{K_z a_z}{\pi} \right)^2 \left(\frac{a_x^2}{a_z^2} \right). \tag{5.8}$$

In practice we always solve for the dimensionless eigenergies $e \equiv E^{(0)}/E_{\text{ISW}}$. Further, because were are now working in three-dimensions we can no longer plot the full bandstructure on two-dimensional sheets of paper (or computer screens). Therefore, we will adopt the usual procedure of tracing out a one-dimensional path through K-space hitting "high-symmetry points" on our trajectory. Following typical convention, we define some of these points (K_x, K_y, K_z) to be $\Gamma = (0, 0, 0)$, $X = (\pi/a_x, 0, 0)$, $M = (\pi/a_x, \pi/a_y, 0)$, and $R = (\pi/a_x, \pi/a_y, \pi/a_z)$.
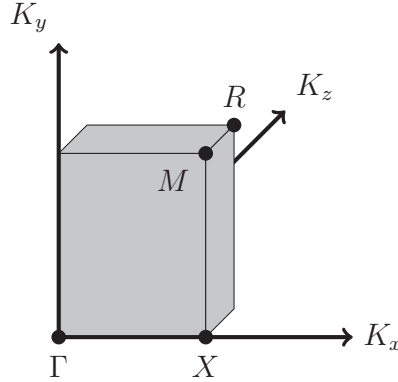
Figure 5.1: Representation in K-space of the location of the high-symmetry points in three dimensions. Similar symmetric points are found in the other seven octants (not shown).

5.2   Simple Cubic or 3D Kronig-Penney Model

Our simplest model is the three-dimensional extension of the Kronig-Penney model: a cubic well of "height" V_0 (with dimensionless value $v_0 \equiv V_0/E_{\text{ISW}}$) located at the center of a cubic unit cell ($a_x = a_y = a_z \equiv a$). V_0 will take on negative values in the region

$$0 \leq q_1 \leq q_2 \leq a \tag{5.9}$$

and will be zero otherwise (at this point we have yet to impose the restriction that the well be located at the center of the unit cell, which requires that q_1 and q_2 be symmetric about $a/2$). In dimensionless form we normalize by our length scale a such that $p_1 = q_1/a$ and $p_2 = q_2/a$, giving

$$0 \leq p_1 \leq p_2 \leq 1. \tag{5.10}$$

Readers familiar with solid state physics will recognize this as a simple model of a *simple cubic* crystal structure. A simple representation of this unit cell is shown in Fig. 5.2.
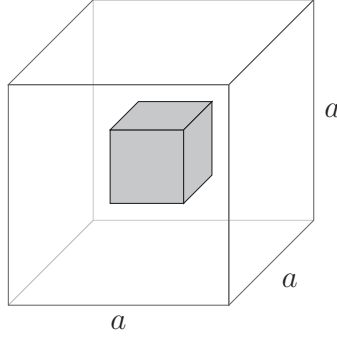
Figure 5.2: Simplified representation of the 3D Kronig-Penney model unit cell.

As we worked out in Section 4.2, by simple extensions the dimensionless matrix elements for this model can be written as

$$h^V_{n_x n_y n_z, m_x m_y m_z} = v_0 I(n_x, m_x) I(n_y, m_y) I(n_z, m_z) \tag{5.11}$$

where

$$I(n_j, m_j) = (p_2 - p_1)\, \delta_{n_j m_j} + i\, \frac{\left(e^{i2\pi(m_j - n_j)p_1} - e^{i2\pi(m_j - n_j)p_2}\right)}{2\pi(m_j - n_j)} \left(1 - \delta_{n_j m_j}\right) \tag{5.12}$$

where $j = x, y, z$. Note that for the main-diagonal terms the contributions will simply be the 4D "volume" $v_0 (p_2 - p_1)^3$.

We show some band structure figures in Fig. 5.3, for $p_1 = 0.25$ and $p_2 = 0.75$ (equal parts well and empty space). The band structure is significantly more complicated than in one- or two-dimensional problems, which is to be expected given the larger number of states.
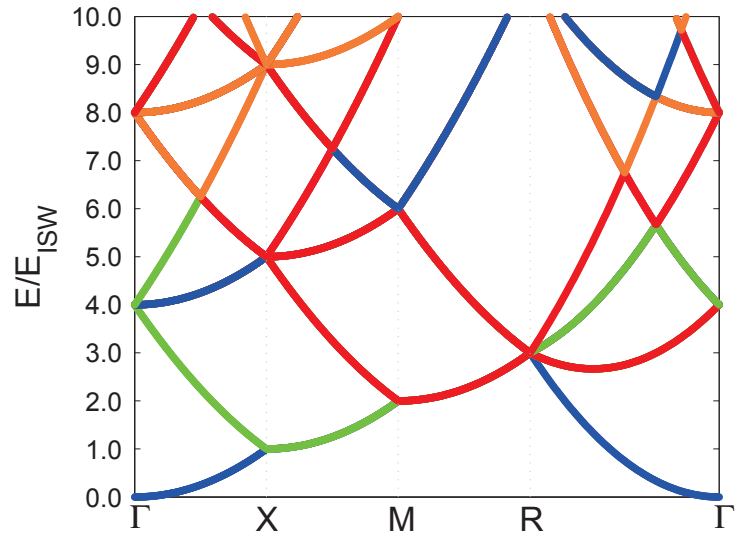
(a) $v_0 = 0$
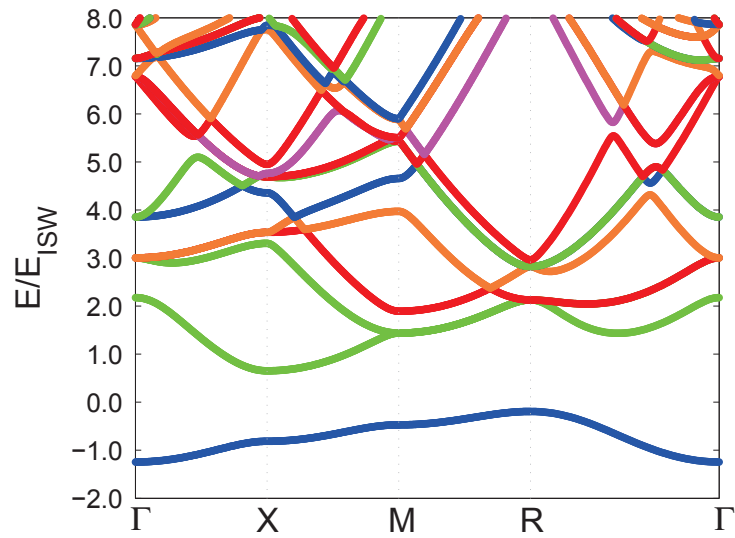
(b) $v_0 = -5$

Figure 5.3: Generated band structures for the 3D Kronig-Penney model with $p_1 = 0.25$ and $p_2 = 0.75$.

5.3 Body-centered Cubic (bcc)

Sticking with cubic wells for simplicity, we can extend our analysis to other crystal systems. In Fig. 5.4 we show a representation of the *body-centered cubic* or bcc unit cell, which is like the simple cubic cell but contains 1/8th of an "atomic site" in each corner giving a total of $(1 + 8(\frac{1}{8})) = 2$ lattice points.

Because of the problem of unfolding, band structures generated from this model would not be altogether enlightening. We are content here merely to sketch out how the problem would be approached with our methodology.
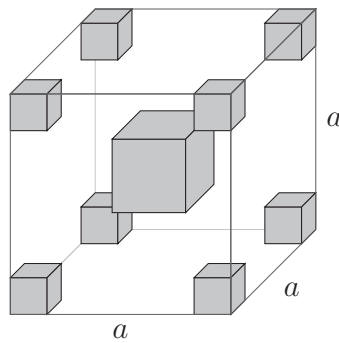
Figure 5.4: Simplified representation of the bcc unit cell.

5.4 Face-centered Cubic (fcc)

In Fig. 5.5 we show the unit cell for the *face-centered cubic* or fcc lattice. Like the bcc unit cell it contains 1/8th-sized wells in the corners, but unlike both the bcc and simple cubic unit cells it does not contain a full central well but 1/2th wells on the "faces" of each of the sides. This gives $(6(\frac{1}{2}) + 8(\frac{1}{8})) = 4$ lattice points.

Similar comments from Section 5.3 apply here as well.

5.5 Other Crystal Systems

While the problem of unfolding is endemic to any approach that does not start from the Wigner-Seitz unit cell, systems that have a rectangular prism unit cell are still perfectly cromulent. We have explored one of these, the simple cubic "3D Kronig-Penney model" which has $a_x = a_y = a_z = a$ side lengths. The two other non-problematic systems are *tetragonal* and *orthorhombic* crystal systems [5].
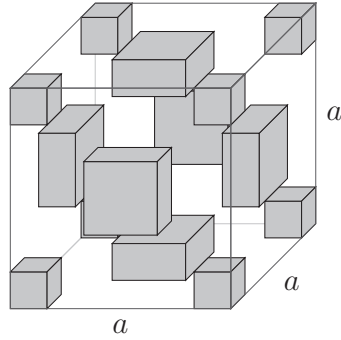
Figure 5.5: Simplified representation of the fcc unit cell.

For tetragonal systems, we have (without loss of generality) $a_x = a_y = a$ and $a_z = b$ where $a \neq b$. In orthorhombic systems none of the side lengths are identical, such that $a_x \neq a_y \neq a_z$. For a one-"atom"-per-unit-cell system, we can simply employ our crude model of Eqs. (5.11) and (5.12) with the energy factors suitably modified as in Eq. (5.8).

Chapter 6

Unfinished Business

In this monograph so far we have demonstrated a method for generating the electronic band structure of bulk crystalline materials in one, two, and three dimensions. As we discovered while investigating two- and three-dimensional systems, however, one naturally encounters the problem of "zone folding" when using rectangular unit cells. In this chapter we reach the current limits of this approach when we look at zone *un*folding. Further, we attempt to introduce electromagnetic terms in the Hamiltonian and discuss problems.

6.1   Unfolding

In Chapter 4 we encountered the problem of non-primitive unit cells generating band structures different from the expected first Brillouin Zone. The difficulty was compounded in Chapter 5 with fcc and bcc lattices. This is a general problem affecting all band structure calculations (not just ours) that use non-Wigner-Seitz unit cells and instead use some more computationally convenient cell (often called supercells).

The use of a non-primitive cell leads to "folded band structures" as we mentioned in Section 4.7. To transform these folded band structures into the first Brillouin Zone band structure, researchers have developed techniques for "zone unfolding" [42]. This process is illustrated in Fig. 6.1.

An in-depth exploration of the mechanics of zone unfolding is outside the scope of this monograph. Computer programs, such as Reference [42], have recently been written to convert given folded band structures into their unfolded forms, and perhaps these programs could be treated like black boxes by students with the input provided by the output of programs written following this present research.

At the present time, however, these programs are simply too complicated to eas-
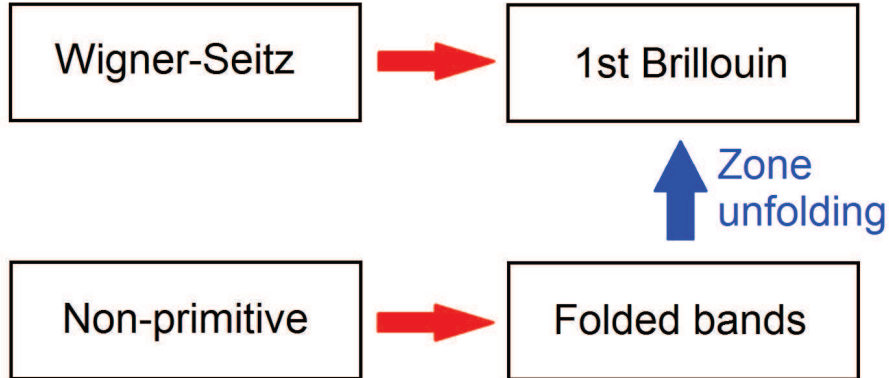
Figure 6.1: Representation of the need for unfolding when using unit cells that are not the Wigner-Seitz primitive cell.

ily be supplied with a student's own input. The program `Quantum Unfolding` [42] requires extensive knowledge of the operations and file structures of `Wannier90` [37], to the extent that in order to use it one would know enough to just generate the band structures from `Wannier90` *de novo*.

That said, the methodology we've developed does allow us to understand folded band structures like Fig. 4.8 at a more than superficial level. While different, there are clear resemblances to the pure free electron Brillouin Zone bands shown in, for example, Fig. 4.3b. What we can do is return to Eq. (4.6) and now treat the ratio a_x/a_y as a parameter and vary it between 1 (Fig. 4.3b) and 2 (Fig. 4.8). We show some of these slices in Fig. 6.2.

It should now be clear what the origin of the various bands in Fig. 4.8 is. One can trace the process where bands move around or previously-degenerate bands split.

While this is useful for supercells that are simple rectangular transformations of the primitive cell, we still have little to say about non-rectangular primitive cells like the hexagonal lattice of Section 4.8.

6.2 Electric and Magnetic Fields

The natural first approach for introducing electric fields (beginning in one dimension) would be to add an electric field term to the one-dimensional Hamiltonian

$$H = -\frac{\hbar^2}{2m_0}\frac{\mathrm{d}^2}{\mathrm{d}x^2} + V(x) + \mathcal{E}x \tag{6.1}$$

(a) $a_x^2/a_y^2 = 1.0$

(b) $a_x^2/a_y^2 = 1.2$

(c) $a_x^2/a_y^2 = 1.4$

(d) $a_x^2/a_y^2 = 1.6$

(e) $a_x^2/a_y^2 = 1.8$

(f) $a_x^2/a_y^2 = 2.0$
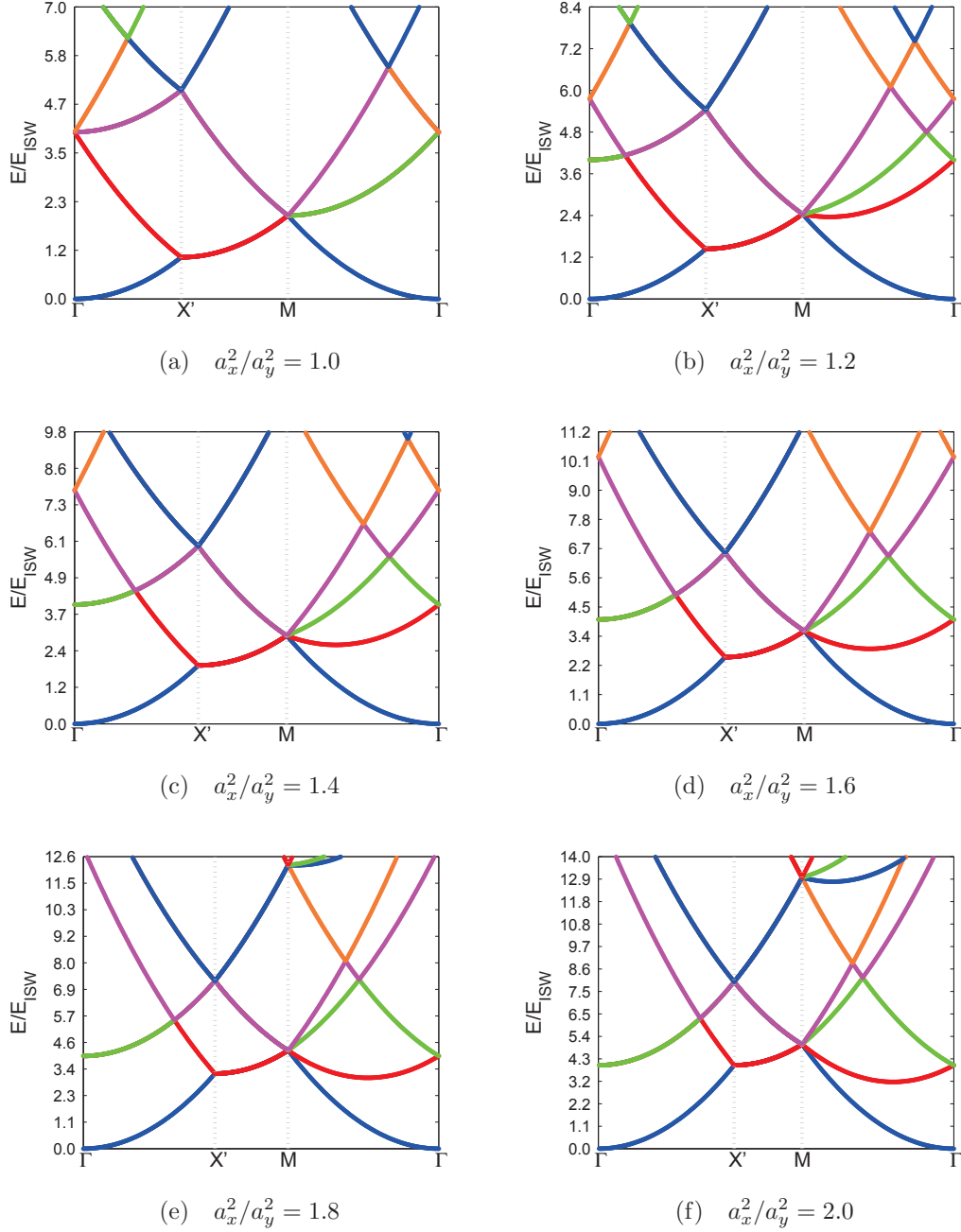
Figure 6.2: Gradually morphing the free electron band structure from the symmetric and familiar $a_x = a_y$ case (compare to Fig. 4.3b) to the $a_x = 2a_y$ case of Section 4.7 (compare to Fig. 4.8).

where $\mathcal{E}$ is the electric field strength in appropriate units. We can see however that when we use our formalism for the one-dimensional Kronig-Penney model the additional factor $\mathcal{E}x$ is applied over one and only one unit cell. The adjacent unit cells are connected mathematically only through Bloch's theorem, and thus naively adding the electric field term will just produce a sawtooth-like pattern, as represented in Fig. 6.3.
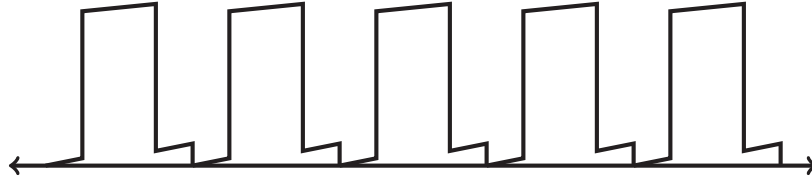
Figure 6.3: Representation of the "sawtooth" nature of naively introducing an electric field term to the one-dimensional Kronig-Penney model.

Even if this naive approach did work, though, there would be another troubling aspect. In Section 2.2 we addressed that, while our lattice was infinite in extent, this was an infinite *extrinsic* magnitude and thus was permissible. However, the electric field term diverges as x approaches positive or negative infinity, and this constitutes an infinite *intrinsic* magnitude which is forbidden (again, Ref. [20] lucidly discusses this dichotomy). While an actual lattice contains a very large number of unit cells, their small size permits the application of electric fields familiar to the human scale (on the order of ∼0.1–1000 V). "Very large" simply isn't infinite.

Another approach might be to use Eq. (6.1) but only on a finite lattice size we discussed in Section 3.6. Then the electric field remains finite in magnitude at the extremes. This approach was taken in Ref. [28], Section IIIE, and is illustrated in Fig. 6.4.
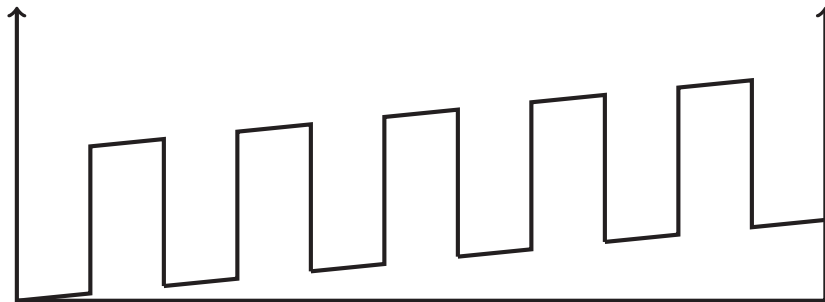
Figure 6.4: Representation of introducing a simple electric field to the "multiple wells embedded in an infinite square well" potential that was discussed in Section 3.6.

In Ref. [28] they found that the "effect of the field consists of the reduction of the forbidden band widths with increasing field strength; eventually, for strong enough

fields, the forbidden bands disappear." While in broad strokes we agree with the physical results, the model remains problematic. In an actual crystal with an imposed electric field, the surfaces of the lattice would be connected to leads that pass through an energy source like a battery. In this model, however, the electron wavefunction redistributes towards the trough, analogous to water in a a tilted glass.

A more realistic model would be dynamical, with electrons being extracted from the low side of the potential and being introduced to the high side (perhaps modelled as simple plane waves). As our method is static, it is not clear how to render it dynamical.

Similarly, magnetic fields ($\mathbf{B}$) are introduced to the Hamiltonian as a position-dependent vector potential ($\mathbf{A}$), since $\mathbf{B} = \nabla \times \mathbf{A}$. We therefore have the same problem as the electric field case for an infinitely-extended lattice, as $\mathbf{A}$ will diverge.

It's however plausible that we can introduce a magnetic field to a restricted lattice, as unlike the case of an electric field the electrons remain bound to the lattice. The Hamiltonian for an electron in the presence of a magnetic field is

$$H = \frac{1}{2m_0} \left(\mathbf{p} - \frac{e}{c}\mathbf{A}(\mathbf{r}) \right)^2 + V(\mathbf{r}) \tag{6.2}$$

where e is the electric charge. Expanding the square and making use of the Coulomb gauge $\nabla \cdot \mathbf{A} = 0$ this gives

$$H = -\frac{\hbar^2}{2m_0}\nabla^2 + \frac{ie\hbar}{m_0 c}\mathbf{A} \cdot \nabla + \frac{e^2}{2m_0 c^2}\mathbf{A}^2 + V. \tag{6.3}$$

Because the force on the electron occurs at right angle to the direction of the magnetic field, there's not much interesting to say about systems where the electrons are confined to one dimension. In two dimensions with the magnetic field perpendicular to the plane ($\mathbf{B} = (0, 0, B)$), the case of free electrons ($V = 0$) famously gives rise to cyclotron orbits with quantized *Landau levels* (see for example Ref. [3]) which have quantum harmonic oscillator energies $\hbar\omega_c \left(n + \frac{1}{2}\right)$ with a *cyclotron frequency* $\omega_c = eB/m_0 c$.

To see this we define a magnetic vector potential $\mathbf{A}$ for our magnetic field in a symmetric gauge

$$\mathbf{A} = \frac{B}{2} \begin{pmatrix} -y \\ x \\ 0 \end{pmatrix}. \tag{6.4}$$

Then, for Eq. 6.3 with $V = 0$ we get

$$H = -\frac{\hbar^2}{2m_0}\nabla^2 + \frac{ie\hbar}{m_0 c}\frac{B}{2}\left(-y\partial_x + x\partial_y\right) + \frac{e^2}{2m_0 c^2}\frac{B^2}{4}\left(x^2 + y^2\right). \qquad (6.5)$$

Recalling the definition for the angular momentum operator L_z

$$L_z = -i\hbar\left(x\partial_y - y\partial_x\right) \qquad (6.6)$$

we can simplify this to

$$H = \frac{1}{2m_0}\left(-\hbar^2\nabla^2 + \frac{ie\hbar}{c}\frac{B}{2}L_z + \frac{e^2}{2c^2}\frac{B^2}{4}\left(x^2 + y^2\right)\right). \qquad (6.7)$$

Now we redefine using so-called magnetic units, using $\omega_c = eB/m_0 c$ as before and $\ell_B^2 = \hbar/m_0\omega_c$. Then we define $x' = x/\ell_B$, $y' = y/\ell_B$, and $\ell_z = L_z/\hbar$ and then drop the primes for convenience (bearing in mind that we are now in magnetic units). Thus, we finally arrive at

$$h_B \equiv \frac{H}{\hbar\omega_c} = -\frac{1}{2}\left(\nabla^2 + \ell_z\right) + \frac{x^2 + y^2}{8}. \qquad (6.8)$$

We can clearly see this is a Hamiltonian for a two-dimensional parabolic potential (hence the harmonic oscillator energy solutions) with an additional contribution from the angular momentum operator.

Nowhere here have we supposed any kind of boundary. If we were to place a parabolic potential in a two-dimensional system with open boundary conditions, we should also want to define it such that our x and y are situated at the center of the well. It is possible that for a high quantum number n (the classical limit), one would find the eigenfunctions taking on the form of the cyclotronic Landau levels.

As this problem does not involve periodic boundary conditions or band structure, it is outside the purview of this monograph, and is left as a challenge for future students to explore. An extension of the problem would be to return to Eq. 6.3 and introduce an actual lattice of (say rectangular) wells for the potential V, and see how that affects matters.

Chapter 7

Conclusion

In this chapter we summarize what we have accomplished and provide an outline pedagogical plan to incorporate our matrix mechanics method into a standard quantum mechanics education.

7.1   Brief Recap

In this monograph we have developed a matrix mechanics approach to calculating the electronic band structure of periodic lattices. It builds on work begun by Marsiglio [8] to increase the use of matrix mechanics in undergraduate quantum mechanics education, as matrix mechanics forms a natural fit with modern fast computers and mathematical software. The goal is a tight coupling between computational results and intuition formation.

In one dimension, we solve for matrix elements using basis states for a periodic unit cell (plane waves). We can then extend this procedure to the full periodic lattice just with additive main diagonal elements, corresponding to the Bloch condition. This allows us to "sweep out" the electronic band structure by repeatedly diagonalizing matrices for different values of the wave vector. With this machinery, one can explore various limits like the nearly free electron model and tight binding, as well as compare electron and hole effective masses for different lattice shapes.

This procedure can then be extended to rectangular and rectangular prism unit cells in two and three dimensions, respectively, though one encounters the problem of folded band structures that are intrinsic to methods that don't use the Wigner-Seitz primitive cell. Nevertheless, the ability for students to generate their own band structures for even simple lattices in these higher dimensions in a direct way is a substantial improvement over existing pedagogy.

7.2 A Possible Curriculum Outline

As the aim of this research is pedagogical, we end by offering an outline for how this research can be fit to undergraduate quantum mechanics courses. This is heavily based on actual practice by Marsiglio in the courses PHYS 372 and PHYS 472 at the University of Alberta.

1. After the introduction of the Schrödinger equation, the eigenfunctions of the infinite square well are found in the usual way.

2. These eigenfunctions can then serve as the basis states for embedding potential of interest, like the harmonic oscillator, in the infinite square well, as discussed in Reference [8]. Perturbation theory notation is used, but if that hasn't been covered in the course yet it's not a great hindrance.

3. With the methodology established for familiar potentials, the double well can be introduced as in Reference [9]. The effect of small asymmetries on such potentials, as in Reference [15], can now be optionally investigated.

4. This procedure can then be extended to more than two wells, perhaps ten. We discussed this approach in Section 3.6 and it is explored further in Reference [28]. In this way students see the natural emergence of energy bands from a solid foundation.

5. The analytical solutions to the Kronig-Penney model can then be developed in the usual way, as we briefly reviewed in Section 2.3.

6. With both a firm understanding of matrix mechanics and knowledge of the Kronig-Penney model, the full machinery of Chapter 3 can be developed, allowing explorations of more realistic potentials.

7. The gap to solid state physics can then be bridged with the subsequent material of this monograph. Then when students encounter new models like the nearly free electron model and tight binding, they will possess a strong point of comparison.

7.3 Research Questions Revisited

In Section 1.2 we enumerated some of the questions used to guide this research. We conclude this monograph by briefly revisiting them:

1. **Can a matrix mechanics approach, hitherto confined to finite potentials, be extended to a periodic lattice (using Bloch's theorem) of arbitrary unit cell potentials?**

   Yes. This was accomplished by using periodic boundary conditions for the unit cell and then introducing the Bloch condition as an additive element to the main diagonal of the Hamiltonian matrix. One can then solve for unit cell matrix elements of whatever (mathematically sound) potential one chooses.

2. **If so, can such an approach be extended to higher dimensions?**

   Yes. By extending our one-dimensional unit cell to rectangular cells and rectangular prism cells, the jump to higher dimensions was accomplished fairly simply. However, one runs into the problem of folded band structure when the Wigner-Seitz primitive cells of the lattice differ from rectangular cells. This was a problem we could not overcome in this present research.

3. **Are there tangible advantages to using such an approach over orthodox methods (nearly free electron model and tight binding)?**

   We believe so. Ultimately this question can only be decisively answered by future generations of students and teachers, but we feel this approach fills a gap in current solid state physics pedagogy. Provided students have some solid grounding in the matrix mechanics approach, if nothing else it serves as a "first pass" for problems in electronic band structure. Marsiglio has stated that he prefers our introductory approach to the hexagonal lattice (Section 4.8) over existing pedagogy, for example.

Bibliography

[1] R. de L. Kronig; W. G. Penney, "Quantum Mechanics of Electrons in Crystal Lattices," Proc. R. Soc. Lond. A, **130**, 499 (1931).

[2] F. Bloch, "Über die Quantenmechanik der Elektronen in Kristallgittern," Z. Physik. **52**, 545 (1929), in German. Remarkably, he has 12 papers that are more cited than this one. See also F. Bloch, "Memories of electrons in crystals", Proc. R. Soc. Lond. A **371**, 24 (1980), where he provides some context for this theorem.

[3] D. J. Griffiths, *Introduction to Quantum Mechanics*, 2nd ed. (Pearson/Prentice Hall, Upper Saddle River, NJ, 2005).

[4] C. Kittel, *Introduction to Solid State Physics*, 7th ed. (John Wiley & Sons, New York, NY, 1996).

[5] N. W. Ashcroft and N. D. Mermin, *Solid State Physics*, 1st ed. (Brooks/Cole, Belmont, CA, 1976).

[6] J. Singleton, *Band Theory and Electronic Properties of Solids*, 1st ed. (Oxford University Press, New York, NY, 2001).

[7] M. Longair, *Quantum Concepts in Physics*, (Cambridge University Press, Cambridge, UK, 2013).

[8] F. Marsiglio, "The harmonic oscillator in quantum mechanics: A third way," Am. J. Phys. **77** (3), 253–258 (2009).

[9] V. Jelic and F. Marsiglio, "The double-well potential in quantum mechanics: a simple, numerically exact formulation," Eur. J. Phys. **33** 1651–1666 (2012).

[10] W. Stacey and F. Marsiglio, "Why is the ground-state electron configuration for lithium $1s^2 2s$?" EPL **100** 43002 (2012).

[11] B. A. Jugdutt and F. Marsiglio. "Solving for three-dimensional central potentials using numerical matrix methods," Am. J. Phys. **81** (5) 343–350 (2013).

[12] J. Hutchison, M. Baker, and F. Marsiglio, "The spectral decomposition of the helium atom two-electron configuration in terms of hydrogenic orbitals," Eur. J. Phys. **34** 111-128 (2013).

[13] L. Forestell and F. Marsiglio, "The importance of basis states: an example using the hydrogen basis," Can. J. Phys. **93** 1009-1014 (2015).

[14] R. L. Pavelich and F. Marsiglio, "The Kronig-Penney model extended to arbitrary potentials via numerical matrix mechanics," Am. J. Phys. **83** (9), 773–781 (2015).

[15] T. Dauphinee and F. Marsiglio, "Asymmetric wave functions from tiny perturbations," Am. J. Phys. **83** (10), 861–866 (2015).

[16] R. L. Pavelich and F. Marsiglio, "Calculation of 2D electronic band structure using matrix mechanics," arXiv:1602.06851.

[17] M. Na and F. Marsiglio, "Two and three particles interacting in a one-dimensional trap," arXiv:1604.01661.

[18] G. Lindfield; J. Penny, *Numerical Methods: Using MATLAB*, 3rd ed. (Academic Press, Waltham, MA, 2012), pp. 135–138.

[19] E. Gkioulekas, "Algorithms with Matlab,"
`faculty.utpa.edu/gkioulekase/codes/matlab_lalg.pdf`, pp. 12–16.

[20] M. Huemer, *Approaching Infinity*, (Palgrave Macmillan, New York, NY, 2016).

[21] Online Encyclopedia of Integer Sequences, "A001057,"
`https://oeis.org/A001057`.

[22] S. Mahajan, *Order of Magnitude Physics: A Textbook, with Applications to the Retinal Rod and to the Density of Prime Numbers*, (Doctoral dissertation). California Institute of Technology, CA. (1998).

[23] T. Pang, *An Introduction to Computational Physics*, 2nd ed. (Cambridge University Press, Cambridge, 2006), p. 51.

[24] P. Nahin, *Inside Interesting Integrals*, 1st ed. (Springer, New York, 2015). Nearly every page is positively bleeding with Nahin's thrill for the act of computation.

[25] J. E. Hirsch, "Dynamic Hubbard Model," Phys. Rev. Lett. **87**, 206402-1–4 (2001).

[26] G. H. Bach, J. E. Hirsch, and F. Marsiglio, "Two-site dynamical mean field theory for the dynamic Hubbard model," Phys. Rev. B **82**, 155122-1–15 (2010), and references therein.

[27] I.D. Johnston and D. Segal, "Electrons in a crystal lattice: A simple computer model," Am. J. Phys. **60**, 600 (1992).

[28] F. Le Vot, *et al.*, "Numerical matrix method for quantum periodic potentials," Am. J. Phys. **84**, 426 (2016).

[29] Z. Liu, J. Wang and J. Li, "Dirac cones in two-dimensional systems: from hexagonal to square lattices," Phys. Chem. Chem. Phys. **15**, 18855 (2013).

[30] Wolfram, Mathematica, `www.wolfram.com/mathematica/`.

[31] Wolfram, Mathematica function `Erf`,
`https://reference.wolfram.com/language/ref/Erf.html`.

[32] MathWorks, MATLAB, `www.mathworks.com/products/matlab/`.

[33] Mathworks, MATLAB function `eig`,
`www.mathworks.com/help/matlab/ref/eig.html`.

[34] Mathworks, MATLAB function `erf`,
`www.mathworks.com/help/matlab/ref/erf.html`.
However, in practice we use Mathworks, MATLAB function `erfi`,
`http://www.mathworks.com/help/symbolic/erfi.html` as the `erf` function does not allow for complex inputs.

[35] Mathworks, MATLAB function `integral2`,
`www.mathworks.com/help/matlab/ref/integral2.html`.

[36] Mathwords, MATLAB function `fit`,
`http://www.mathworks.com/help/curvefit/fit.html`.

[37] Wannier Developer's Group, Wannier90, `www.wannier.org/`.

[38] T. B. Boykin, N. Kharche and G. Klimeck, "Non-primitive rectangular cells for tight-binding electronic structure calculations," Physica E **41**, 490 (2009).

[39] A. H. Castro Neto *et al.*, "The electronic properties of graphene," Rev. Mod. Phys. **81**, 109 (2009).

[40] M. Farjam, "Projection operator approach to unfolding supercell band structures," arXiv:1504.04937v3 (2015).

[41] S. Reich, *et al.*, "Tight-binding description of graphene," Phys. Rev. B. **66**, 035412 (2002).

[42] F. Zheng, P. Zhang and W. Duan, "`Quantum Unfolding`: A program for unfolding electronic energy bands of materials," Comput. Phys. Commun. **189**, 213-219 (2015).

[43] Digital Karnak Project, "Hypostyle Hall,"
`http://dlib.etc.ucla.edu/projects/Karnak/feature/HypostyleHall`.